Chair of Functional Materials and Materials Systems

Master's Thesis

Sputter deposited SnOx films for gas sensors

Maximilian Preindl, BSc

September 2020

MONTANUNIVERSITÄT LEOBEN
www.unileoben.ac.at

EIDESSTATTLICHE ERKLÄRUNG

Ich erkläre an Eides statt, dass ich diese Arbeit selbständig verfasst, andere als die angegebenen Quellen und Hilfsmittel nicht benutzt, und mich auch sonst keiner unerlaubten Hilfsmittel bedient habe.

Ich erkläre, dass ich die Richtlinien des Senats der Montanuniversität Leoben zu "Gute wissenschaftliche Praxis" gelesen, verstanden und befolgt habe.

Weiters erkläre ich, dass die elektronische und gedruckte Version der eingereichten wissenschaftlichen Abschlussarbeit formal und inhaltlich identisch sind.

Datum 16.09.2020

Preindl Maximilian

Unterschrift Verfasser/in
Maximilian, Preindl

Acknowledgments

My sincerest gratitude is due to Univ. Prof Dipl. Ing. Dr. mont. Christian Mitterer, Head of the Chair of Functional Materials and Materials Systems, for providing me the opportunity of writing this thesis under his supervision, for his patience and the confidence he placed in me.

I would like to thank Univ. Doz. Mag. Dr. Anton Köck and his team from the Materials Center Leoben for giving me the financial support by the project "Innovative Chemical Nano-Sensors for Safety Applications in Homes and Industry" – NanoSense and their support during my work. Thanks go to the MCL for carrying out FIB, SEM and AFM investigations and the gas sensitivity measurements.

Big thanks and hugs go to Veli (Velislava Terziyska) for introducing me in the laboratory and giving tons of helpful advises during my work. Without her guidance, valuable inputs and encouragement it would not have been possible to write this work. I would like to thank her for the countless hours she spent teaching and supporting me as a supervisor and as a friend.

Thanks go to all members of the thin film group for the support and advises whenever needed and the pleasurable atmosphere. A special thanks go to Nikos (Dr. Nikolaos Kostoglou) and Anna (Dr. Anna Hofer-Roblyek) for their helpful advises and support.

I am grateful to Dr. Frans Munnik from the Helmholtz-Center Dresden-Rossendorf for carrying out the ERDA measurements.

Thanks go to all my friends I found in Leoben for the great time we had and the unforgettable memories we made. Special thanks go to Boris and Gerhard who are the best flat mates one could imagine. Thanks to my friends at home in South Tyrol for their love and support.

Zu guter Letzt möchte ich meinen allergrößten Dank meiner Familie aussprechen. Nur durch ihre finanzielle und anderweitige Unterstützung war es möglich, dieses Studium zu absolvieren.

Table of Contents

1 Introduction ... 1
2 Theoretical Background ... 3
2.1 Tin Oxide ... 3
2.1.1 Tin ... 3
2.1.2 Oxygen ... 3
2.1.3 Tin Oxides ... 3
2.1.4 Solid-State Gas Sensors ... 6
2.2 Physical Vapor Deposition ... 9
2.2.1 Deposition Technique – Sputtering ... 10
2.2.2 Nucleation and Growth ... 14
2.2.3 Structure Zone Models ... 16
2.3 Nano Cluster Deposition via Gas Phase Synthesis ... 19
2.3.1 Particle Formation ... 20
2.3.2 Particle Growth ... 21
3 Experimental ... 23
3.1 Coating Deposition ... 23
3.1.1 Deposition System ... 23
3.1.2 Target, Substrate Materials and Working Gases ... 24
3.1.3 Deposition Procedure ... 24
3.2 Coating Characterization ... 25
3.2.1 X-Ray Diffraction Analysis ... 25
3.2.2 Raman Spectroscopy ... 26
3.2.3 Elastic Recoil Detection Analysis ... 28
3.2.4 Focused Ion Beam Investigation ... 30
3.2.5 Scanning Electron Microscopy ... 31
3.2.6 Four-Point Resistivity Measurement ... 31
3.2.7 Atomic Force Microscopy ... 32
4 Results and Discussion ... 33

4.1 Film Surface Topography and Morphology 33
4.2 Elemental Composition 36
4.2.1 EDX 36
4.2.2 ERDA 37
4.3 Film Structure and Phase Composition 39
4.3.1 X-Ray Diffraction 39
4.3.2 Raman Spectroscopy 43
4.4 Electrical Resistance 47
4.5 Gas Sensitivity Measurements 49
4.6 Deposition of Au clusters 51
5 Conclusions and Outlook 55
5.1 Conclusions 55
5.2 Outlook 55
References V

1 Introduction

"The advance of technology is based on making it fit in so that you don't really even notice it, so it's part of everyday life" -Bill Gates

The zeitgeist of our generation is, that things have to become smarter, faster, smaller, more energy-efficient and last but not least compatible with existing technology. The necessity to create sensors fulfilling the mentioned tasks is required by fast technological progress. Presently, in particular in the realm of gas sensing, metal oxide solid-state gas sensors are about to replace conventional spectroscopic and optic systems. Tin dioxide (SnO_2) has been found to be a promising material which fulfils the required demands. While solid-state gas sensors are state of the art, future gas sensors will be functionalized by novel metal nano clusters, which have been shown to enhance the performance of the used gas sensing layers [1].

Physical vapor deposition (PVD) has established as one of the most commonly utilized methods to apply coatings and thin films on solid surfaces. PVD processes are atomistic deposition processes based on the condensation of particles from the vapor phase [2]. PVD provides the ability to fabricate clean thin films without contamination with organic material and is consequently an ideal method to process gas sensing layers for e.g. carbon monoxide.

The recently introduced gas phase synthesis using magnetron sputter inert gas condensation provides a wide variety in nano cluster materials and an excellent control in their size, density and morphology, once the different kinetic and thermodynamic contribution to the formation and growth of nano clusters are well understood [3].

The aim of this work is to develop tin oxide thin films synthesized via reactive DC magnetron sputtering in an argon oxygen atmosphere and to characterize them with respect to structure, phase composition and chemical composition. The attempt was made to use different working gas compositions at different processing temperatures with the goal to understand the influence of the process parameters on the film's characteristics. Further Au nano clusters were deposited on selected samples and characterized in size, distribution and topography. The task of this work is on one hand to find the right process parameters to grow SnO_2 thin films for the use as solid state gas sensors. On the other hand, to deposit Au nano clusters via

gas phase synthesis and investigate them in order to obtain an understanding of the growth process as well as to correlate the process parameters with cluster properties.

2 Theoretical Background

2.1 Tin Oxide

2.1.1 Tin

Tin with the chemical symbol Sn (from Latin: Stannum) is a p-block element with the atomic number 50. Tin is forming a centered tetragonal structure with lattice constants of 583.18 pm, 583.18 pm and 318.19 pm. At standard conditions, tin which is of silver color, has a density of 7.31 g/cm^3. It is mainly obtained from the mineral cassiterite, which contains stannic oxide SnO_2 [4].

2.1.2 Oxygen

Oxygen is a chemical element with the symbol O. It is a p-block element, which at standard conditions forms a colorless, odorless diatomic gas with the formula O_2. With 21 vol.-%, oxygen represents a main fraction of air and plays an essential role in nearly all biological processes. Oxygen is a highly reactive element: oxygen atoms react spontaneously with atoms of all elements except noble gases and form polyatomic molecules via covalent bonds [5].

2.1.3 Tin Oxides

There are two main types of tin oxide: stannous oxide (tin monoxide, SnO) and stannic oxide (tin dioxide, SnO_2). The existence of these two oxides reflects the dual valence of tin, with oxidation states of 2+ and 4+. Stannic oxide possesses the rutile structure, whereas stannous oxide forms the less common litharge structure [6]. **Figure 2.1** shows the Sn-O phase diagram for atmospheric pressure. The diagram indicates also the presence of an intermediate tin-oxide phase between SnO and SnO_2. The Sn_3O_4-phase indicated in **Fig. 2.1** is often given for its composition [7], but also Sn_2O_3 has been considered [8, 9].

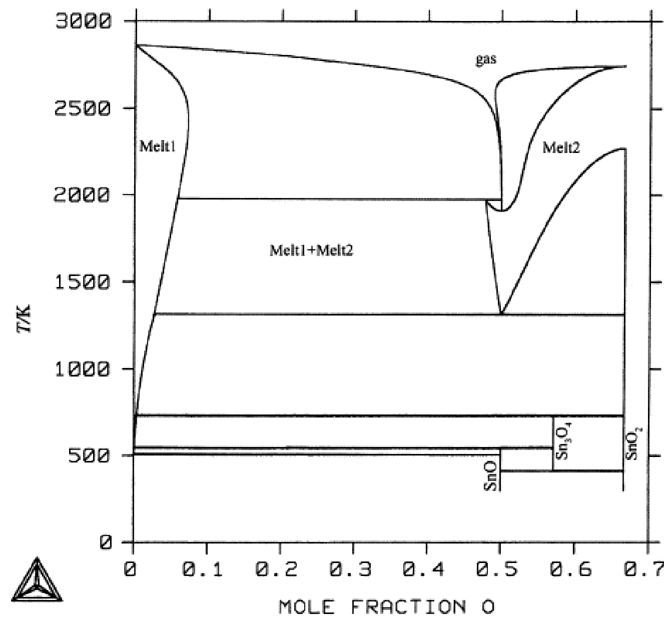

Figure 2.1: Sn-O phase diagram calculated at 1 bar [10].

In fact, the structure of SnO is not that well known and characterized than SnO_2. Stannous oxide has a tetragonal unit cell with a litharge structure, isostructural to PbO (**Fig. 2.2**). The lattice parameters are a = b = 3.8029 Å and c = 4.8382 Å [11]. Each Sn and O atom is fourfold coordinated with a bond length of 2.23 Å. The structure is layered in the [001] crystallographic direction with a Sn1/2–O–Sn1/2 sequence and a van-der-Waals gap between two adjacent Sn planes of 2.52 Å [6]. Tin monoxide is reported to be a p-type semiconductor with a fairly high hole mobility among p-type conductive oxides reported to date [12] and is therefore a promising material for thin film transistors. The origin of p-type conductivity of SnO is attributed to Sn-vacancies, which form preferentially under oxygen-rich conditions [13]. In this situation, some cations will be transformed to Sn^{3+} to maintain charge neutrality, equivalent to a Sn^{2+} ion and a weakly bonded hole [14]. The bandgap is not accurately known and lies somewhere between 2.5 and 3 eV [6]. During PVD, slight variations of the deposition conditions may result in mixed phases of SnO with metallic Sn and/or SnO_2 leading to irregular electrical conduction in the deposited films [15, 16]. This is because SnO tends to be oxidized to SnO_2 and decomposes to Sn and SnO_2 above a certain temperature (**Fig. 2.1**), either directly or through the formation of intermediate compounds such as Sn_2O_3 or Sn_3O_4 [7, 8].

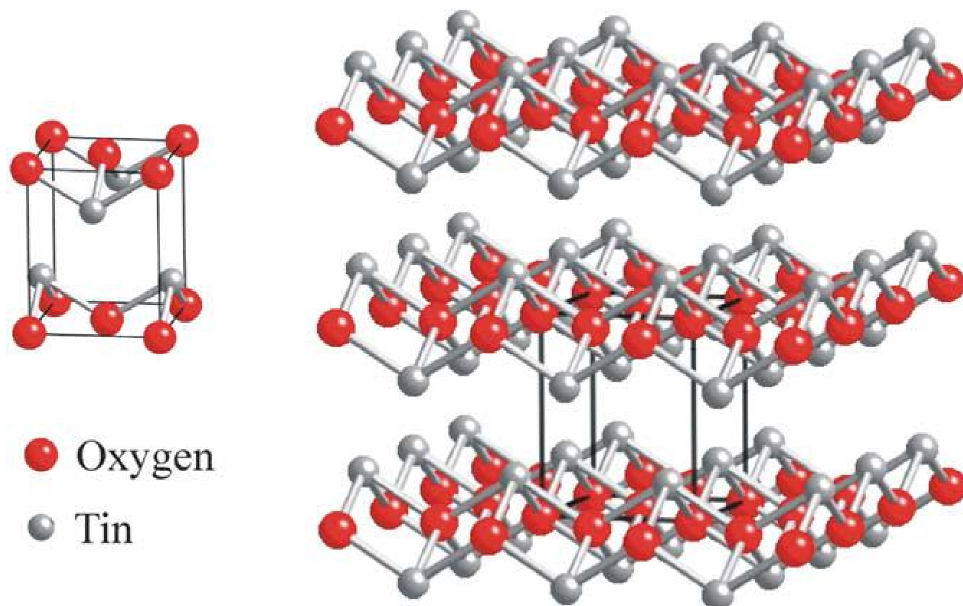

Figure 2.2: Ball-and-stick model of the litharge structure of SnO [6].

Stannic oxide SnO_2 is better characterized than stannous oxide. It possesses the same rutile structure as many other metal dioxides, e.g. TiO_2, RuO_2, MnO_2, GeO_2, VO_2 and CrO_2 [6]. The rutile structure has a tetragonal unit cell and the lattice constants are a = b = 4.7374 Å and c = 3.1864 Å [17]. The Sn atoms are sixfold coordinated to threefold coordinated O atoms (**Fig. 2.3**). SnO_2 belongs to the family of transparent conductive oxides (TCOs) and combines a relatively high electrical conductivity with a high optical transparency. It is an n-type semiconducting material with a bandgap of E_g = 2.7 eV at 300 K and it is used in transistors, as oxidation catalysts, as transparent conducting electrodes, in solar cells and in gas sensors.

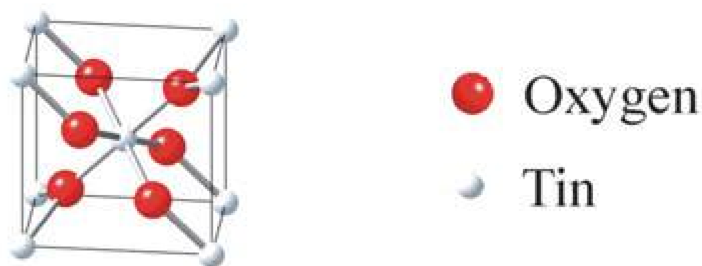

Figure 2.3: Ball-and-stick model of the SnO_2 unit cell [6].

2.1.4 Solid-State Gas Sensors

As the main topic of this thesis is the application of tin oxide in gas sensors, its function as a gas sensing material will be described in detail. A huge number of oxides showing a chemiresistive gas sensing behavior is known of which tin dioxide (SnO_2) is the widest investigated material. The working principle is a change of the solid-state gas sensor materials' properties when the concentration of a specific gas in the ambient atmosphere changes. The change of the materials' properties, i.e. electrical conductivity, is then transformed into a measurable electrical signal. Tin dioxide is widely used as gas sensor material because it shows many advantages compared to other semiconducting metal oxides, such as low costs, good mechanical properties, high reliability, good resistance to corrosive gases and therefore a long operating life. A disadvantage is its sensitivity to nearly all appearing gaseous species in industry, leading to a low selectivity. In addition, due to the sensitivity to H_2O (gas) also a big influence of the ambient humidity has to be expected.

2.1.4.1 Fundamentals of Solid-State Gas Sensors

In fact, the main reason why solid-state gas sensors are used is because they are ways cheaper in production compared to the conventional spectroscopic and optic systems. Furthermore, they are smaller, easier to handle and compatible with complementary metal oxide semiconductor (CMOS) technology, which means they are also less-power consuming than conventional systems [18]. **Figure 2.4** shows the basic design of a semiconductor gas sensor.

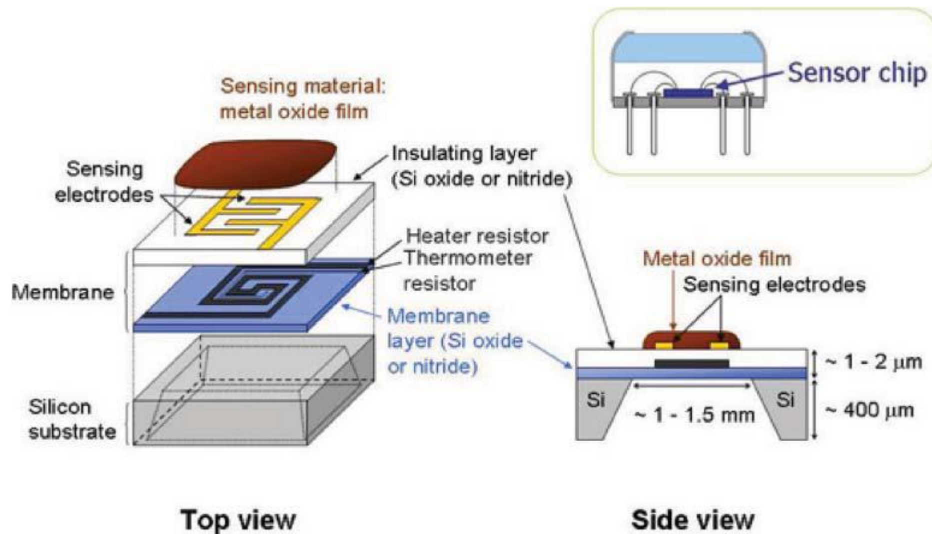

Figure 2.4: The basic sensor consists of a substrate where the sensor material is supported, interdigitated electrodes (to measure the conductivity changes), a measure resistor (to control the sensor temperature) and a heater (to reach the optimum sensing temperature) [18].

In principal, there are three different mechanisms of interaction between a surface and a gas [19]: physisorption due electrostatic forces of nonreactive atoms/molecules (van-der-Waals; dipole/dipole), chemisorption where chemical bonds between the gas atoms and the solid are formed – accompanied by a charge transfer process – and non-reversible reactions which typically result in the formation of a new compound. Since the working principle of solid-state gas sensors is a change in the electrical resistance depending on the gaseous atmosphere the surface is exposed to, chemisorption should be the main interaction mechanism. There are still controversial opinions about the exact underlying procedures, in principle it is a trapping of electrons at the absorbed molecules of the gas atmosphere causing a bending of the bands in the sensing material. When a molecule adsorbs at the surface, electrons can be transferred to this molecule if the lowest lying unoccupied molecular orbitals of the adsorbate complex lie below the Fermi level E_F (acceptor levels) of the solid and vice versa electrons are donated to the solid if the highest occupied orbitals lie above the Fermi-level of the solid (donor levels) [6]. This induces an electrostatic field, which leads to a bending of the energy bands in the solid. A negative surface charge bends the bands upward, i.e. pushes the Fermi level into the band gap of the solid, effectively reducing the charge carrier concentration and resulting in an electron depletion zone (**Fig. 2.5 a**). Further, in a polycrystalline material the surface-near depletion zone due to band bending forms Schottky-like barriers between the grains, which hinder electrons to move easily to the material (**Fig. 2.5 b**).

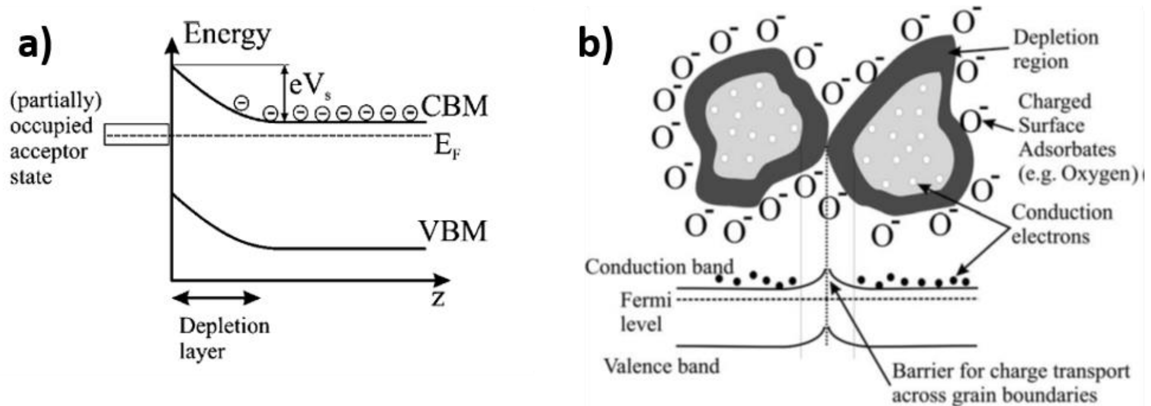

Figure 2.5: **a)** Schematic representation in the near surface region of an n-type semiconductor induced by a (partially) filled donor state of an adsorbed molecule; **b)** Schematic representation of charge carrier concentration in SnO_2 grains [6].
(CBM…conduction band minimum; VBM…valence band maximum)

In general, reducing gases increase the conductivity of the SnO_2 gas sensing material while the opposite is observed for oxidizing gases. Adsorbed negatively charged oxygen species are believed to be responsible for this phenomenon [20].

2.1.4.2 Functionalization of Gas Sensors with Nano Clusters

Over the last decades, nano structured materials have been intensively investigated and have become a serious topic in science. With respect to conventional micro structured materials, nano materials offer a wide range of different mechanical, physical and electrical characteristics, although the chemical composition of the material does not change. Looking at phenomena in nature which base on nano structured surfaces, anybody can imagine e.g. a picture of a gecko, walking along upside down a ceiling. Millions of very thin hairs on its feet with a diameter of below 200 nm providing a giant surface allow the gecko to use weak Van-der-Waals forces to hang upside down on even one single toe, independent on the structure of the surface it is walking on.

Technologists talk about nano materials when structure dimensions, i.e. grain sizes, are 100 nm or below. It has been found that the gas-sensing properties of chemiresistors may be tailored by adding catalytically active nano clusters to the sensor surface, which usually leads to a change of sensitivity, gas selectivity, and response/recovery times [1]. Many species are used to manipulate the properties of the basic material such as noble metals (Au, Ag, Pt, Pd), transition metals (Fe, Co, Co, Ni, Mn) and oxides [21]. Depending on the choice of the material, a different behavior can be expected. As one can imagine, the particle size and shape, but also the number of particles on the surface may affect the catalytic effect of the added material. Via nano particle design by gas phase synthesis, dimensional properties can be specially edited

in order to get the required functionalization of a solid-state gas sensor. Gas phase synthesis and nano cluster deposition is described in detail in section 2.3. **Figure 2.6** shows the response of a SnO_2 gas sensor, once with and once without Pt clusters at the surface, to different concentrations of Co and NO_2.

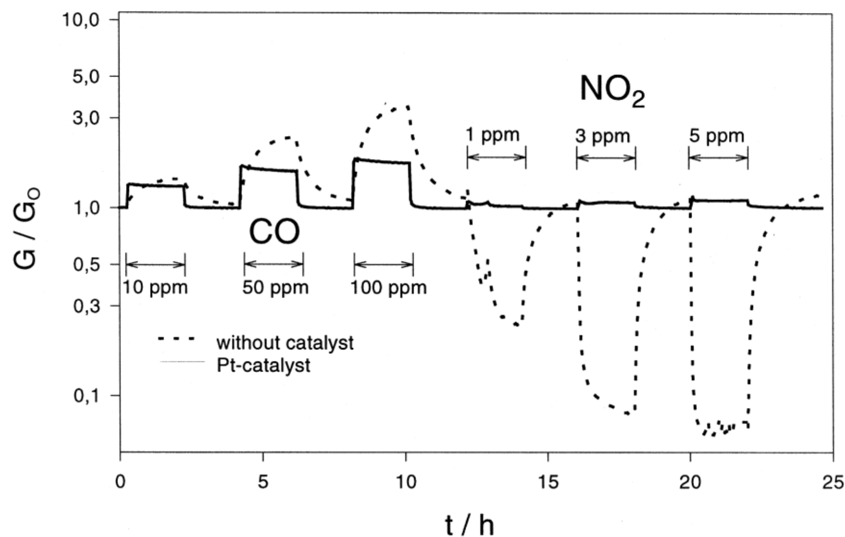

Figure 2.6: Comparison of the normalized response (T = 360 °C, 40% relative humidity) of a SnO_2 thin film sensor with a sensor with Pt clusters at the surface to CO and NO_2 over time [22].

2.2 Physical Vapor Deposition

Physical vapor deposition processes (often just termed thin film processes) are atomistic deposition processes, in which material is vaporized from a solid or liquid source in the form of atoms or molecules and transported in the form of vapor through a vacuum or low pressure gaseous (or plasma) environment to the substrate, where it condenses [2]. PVD processes have been established in thin film technology, as they allow to produce a wide variety of coatings with many different elemental compositions.

In principle, PVD represents a process technology family consisting of four steps: formation of the vapor phase, transport of atoms or molecules to the substrate, deposition on the substrate and rearrangement of the atoms on the substrate surface. According to *Ohring* [23], PVD can be split into two categories distinguished by the mechanism of vapor generation: *evaporation* and *sputtering*. Quite simply in evaporation processes a heat source is used to vaporize the material. The process is usually performed at low pressure of 10^{-8} to 10^{-3} Pa. As a result, the atoms or molecules may reach the target with little or no collisions with the working gas molecules. In some applications, evaporation has been taken over by sputtering, where vaporization of atoms from the surface of a so-called target is reached by ejection of these

atoms due to bombardment with energetic particles – usually energetic ions from a plasma. Sputtering has the advantage to make possible the deposition of refractory metals at relatively low temperatures and high-melting metals and ceramics can be sputtered. It is scalable also for large area deposition. Sputtered films are applicable to all classes of materials [2, 23, 24].

2.2.1 Deposition Technique – Sputtering

2.2.1.1 Fundamentals of Sputtering

The physical sputtering process involves the physical vaporization of atoms from a surface by momentum transfer from bombarding energetic atomic-sized particles [2]. Usually those energetic particles are Ar^+ ions coming from the plasma near the target. The ions are attracted due to the cathode potential applied to the target. In fact, in a sputter deposition system the target represents the cathode and the substrate holder represents the anode. The positive ions arise from a glow discharge between the electrodes; they are then accelerated towards the target surface. The so "knocked out" atoms from the target surface recondense at surfaces inside the vacuum chamber and the substrate. The characteristic number of the sputtering process is the so-called sputter yield S, which is defined as:

$$S = \frac{Atoms\ removed}{Incident\ ions} \tag{1}$$

The sputter yield is influenced by the energy of the incident ions, the incident angles of the ions and the target material and its surface structure [25]. Sputtering is caused by a collision cascade in the surface layers of a solid. The process is activated by the first collision between bombarding ions and the surface atoms, followed by second and third collisions between the target surface atoms. **Figure 2.7** shows the events occurring during ion bombardment of a solid surface.

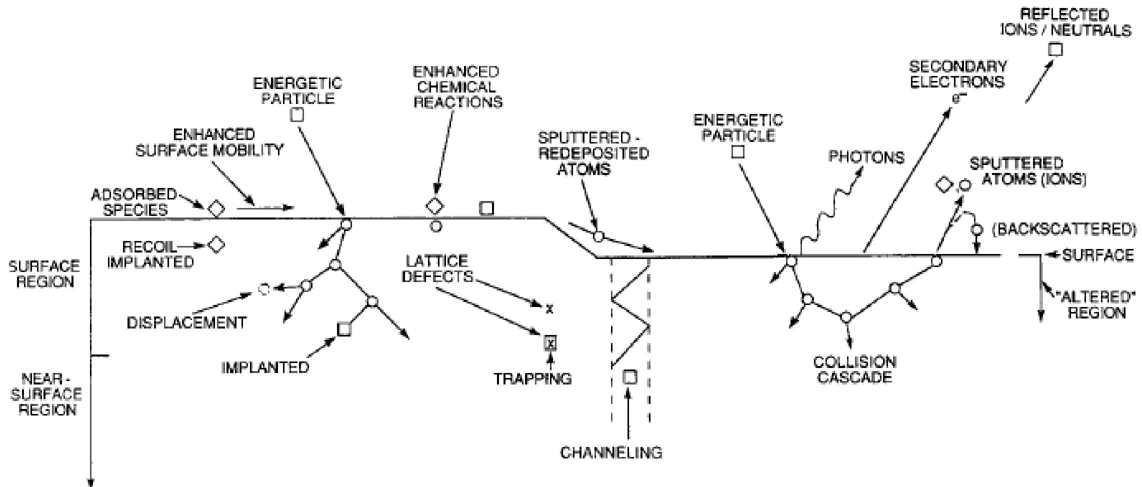

Figure 2.7: Depiction of energetic-particle bombardment effects on surfaces and growing films [23].

2.2.1.2 Diode Sputtering

The direct current (DC) diode setup is the simplest sputtering system. In fact, the configuration consists of a cathode, which is the target, and an anode usually facing each other. The substrate(s) are placed on the anode. During the process, the target fulfills two functions, one as the source of the coating material and another one as the source of secondary electrons. Those secondary electrons are accelerated away from the cathode and create ions, which sustain the glow discharge [2, 26]. A DC diode system with the according distribution of the potential across the discharge is schematically illustrated in **Fig. 2.8**.

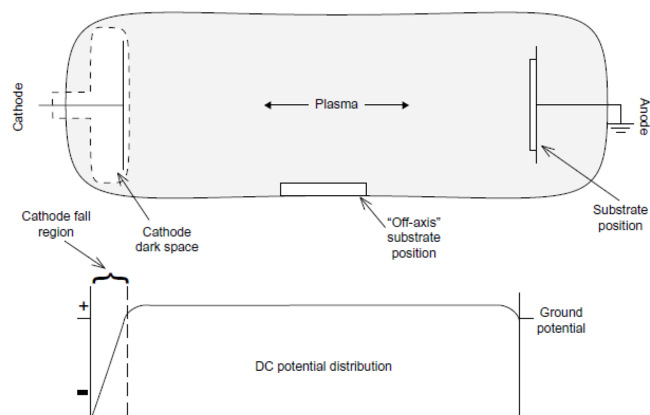

Figure 2.8: Direct current diode discharge showing the potential distribution across the discharge [2].

The working pressure during DC-sputtering is in the range of below 10 Pa. If the pressure is too low, the mean free path of the electrons collected by the anode is large and the electrons

are not supplemented by secondary electrons. As a result, self-sustained discharges cannot be maintained, and ionization efficiencies are too low. On the other hand, if the working pressure is too high, the ejected atoms undergo a higher number of scattering-collisions and consequently the deposition rate diminishes. Because of the high temperatures that occur during the sputtering process, the cathode is usually water cooled [2, 23–25].

2.2.1.3 Magnetron Sputtering

Compared to the DC-diode setup, the use of magnetron devices provides advantages – especially a higher deposition rate. What distinguishes a magnetron cathode from a conventional diode cathode is the superposition of a transversally orientated magnetic field and the electric field. Consequently, the secondary electrons can be deflected and hold on a circular closed path above the target surface, which leads to a denser plasma near the surface and an increase of the ionization efficiency. This leads to lower gas pressure needed to maintain a stable discharge and consequently an increase of the mean free path of the sputtered atoms allowing a higher deposition rate at same electrode spacing and minimum target voltage.

For thin film deposition, there are two different types of magnetron systems widely used. One is a cylindrical type and one – the most common – is the planar type [23]. **Figure 2.9** illustrates a schematic of a rectangular planar magnetron configuration. One can see that the local polarity of the magnetic field is orientated such that the secondary electrons are trapped in a so-called *racetrack* closed loop. Thus, the erosion is concentrated in these areas. The conventional magnetron shown in **Fig. 2.9** is also called balanced [2, 23–27].

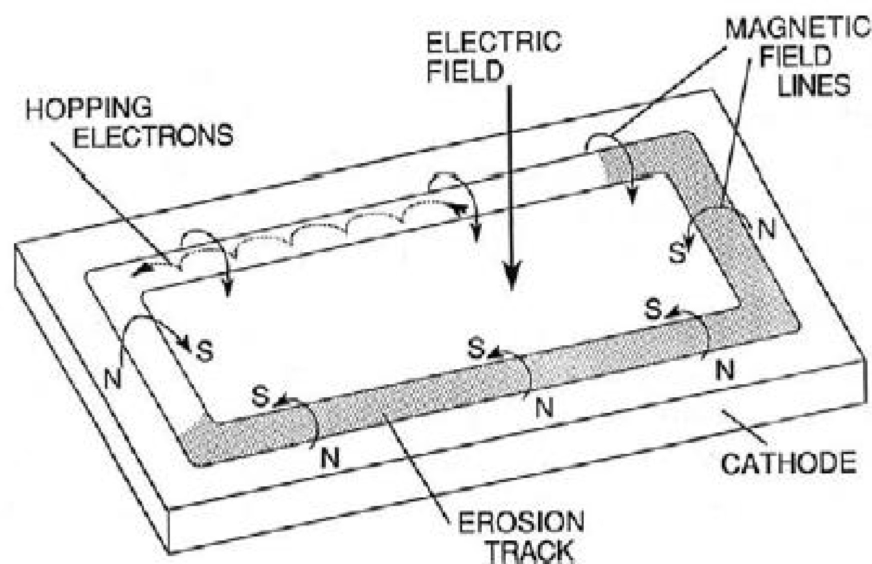

Figure 2.9: Applied fields and electron motion in a planar magnetron [23].

In order to overcome the disadvantage of plasma not being available near the substrate to activate reactive gases for reactive deposition of e.g. oxides and nitrides, unbalanced magnetron configurations can be used. In an unbalanced magnetron, the magnetic field is orientated such that some electrons can escape from the target near region and may generate a secondary plasma near the substrate (**Fig. 2.10**) [2, 25].

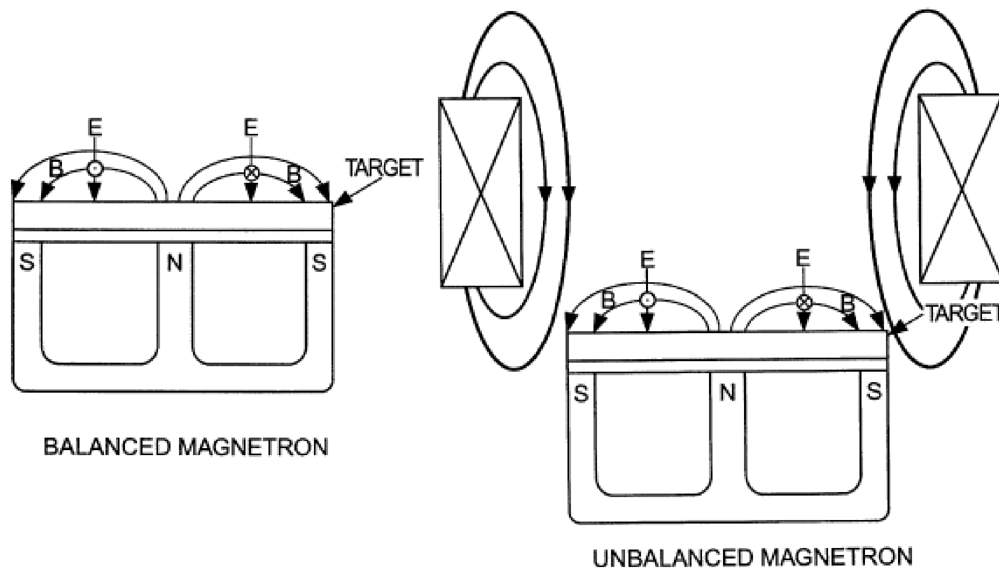

Figure 2.10: Schematic of balanced and unbalanced magnetrons [25].

2.2.1.4 Reactive Sputter Deposition

Magnetron sputtering is a powerful technique to deposit thin films of elemental composition. However, there are methods to deposit alloy films, such as the use of different targets simultaneously, and dielectric films, such as oxides or nitrides, either by sputtering insulating targets using radio frequency power or by reactive sputtering of a metal target [24, 28]. Reactive sputtering is a process where vapor stemming from the target material combines with the component of an added gas phase and consequently films are deposited as a reaction product. The reactive gas is usually introduced in the molecular state, e.g. oxygen as O_2. Typically, the inert gas argon is used for sputtering, due to its sufficiently high atomic mass (40 amu). The frequently used reactive gases have a lower atomic mass (O = 16 amu, N = 14 amu) and thus do not contribute efficiently to sputtering. Mixing argon with the reactive gas results in activation of the reactive gas to form more chemically reactive or more easily adsorbed species (e.g. N, O, N^+, O^+, etc.). The reactions to form the compound may take place either on a solid surface or far more unlikely in the gas phase. The typical problem in reactive sputtering is the so called “poisoning” of the target, by the formation of a compound of the reactive gas

and the target material at the target surface. Poisoning decreases the sputter rate and is not desirable. The common way to deal with this problem is to control the reactive gas flow so that there is enough reactive species to react with the film surface, but not so much that they will poison the target. To achieve this, the inlet of the reactive gas is usually near the substrate, whereas the inert gas inlet is near the target. Further, using unbalanced magnetrons the plasma can be enlarged and intensified in the substrate near area [2, 23–28]. The configuration of a reactive sputtering chamber is shown in **Fig. 2.11**.

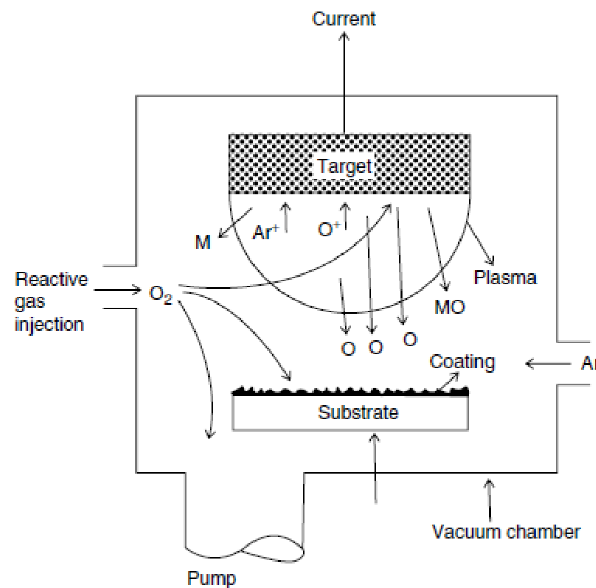

Figure 2.11: Schematic of a reactive sputtering chamber [24].

2.2.2 Nucleation and Growth

After the first two steps *evaporation* and *atom transport* through the vacuum chamber, condensation, *nucleation and growth* to continuous films take place. Since the impinging atoms and the substrate surface are usually different substances, they do not fulfill the requirements for immediate condensation. In fact, they become weakly bonded atoms termed *adatoms*. These adatoms have a certain mobility through diffusion and may - depending on their energy, the substrate temperature and their interactions with the substrate surface - either be reflected immediately, re-evaporate or be trapped at low energy lattice sites (**Fig. 2.12**) [25].

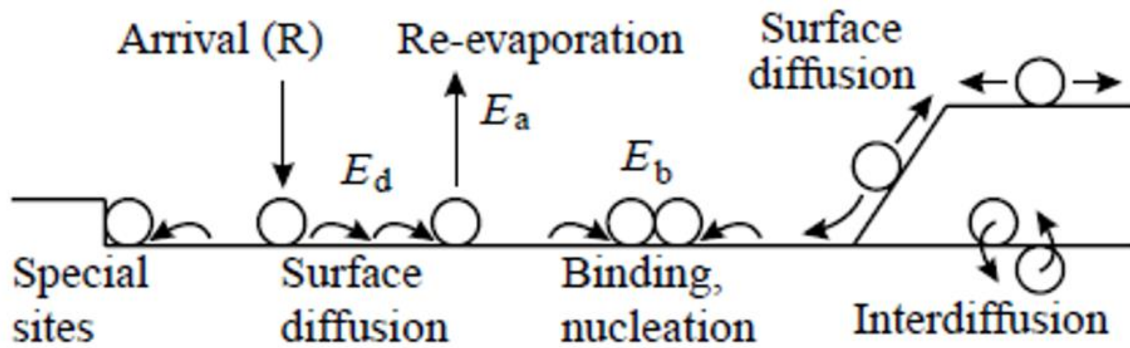

Figure 2.12: Growth model of a thin film [29].

The trapping strongly depends on the surface morphology. Discontinuities such as steps or scratches may act as low energy lattice sites, but also the substrate surface roughness plays an important role. On the other hand, also the microstructure and surface chemistry influence the trapping of the impinging atoms, e.g. by lattice defects, grain boundaries, surface areas with different crystallographic orientation and chemistry. Initially the adsorbed species are not in thermal equilibrium with the substrate and move via diffusion over the surface, until they either desorb or collide with other adatoms and form unstable *nuclei*. When these nuclei reach a certain critical size, they become thermodynamically stable and continue to grow. This so-called *nucleation stage* is followed by the growth of the nuclei in size as well as in number, until a saturation nucleation density is reached. Nuclei grow parallel to the substrate surface, as well as perpendicular to it. This stage is followed by the *coalescence stage*, in which the islands start to grow together and to form bigger agglomerates. When these agglomerates start coalescing, they form a porous network. They leave channels and holes of uncovered substrate which are then successively filled, and a continuous film is formed. Depending on the thermodynamic parameters of the deposit and the substrate, three basic growth modes can be distinguished (**Fig. 2.13**): Volmer-Weber mode (island growth), Frank-Van der Merwe mode (layer growth) or Stranski-Krastanov mode (mixed layer-island growth) [24, 25, 29, 30].

Usually, there is a difference in the crystallographic orientation of the islands and as they touch each other, defects like grain boundaries and several other point and line defects, such as dislocation lines, stacking faults, micro twins, twin boundaries, etc., are introduced. After the formation of a continuous film, an anisotropic growth takes place normal to the substrate surface. Atomistically deposited films in general show a columnar morphology that resembles a logs and plates lined together. These columns are not single crystal grains but generally amorphous or polycrystalline [2, 29].

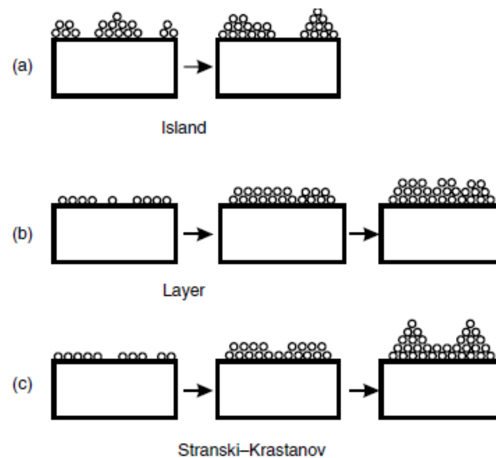

Figure 2.13: Modes of growth of a film. **(a)** Volmer-Weber island growth, **(b)** Frank-Van der Merwe layer growth and **(c)** Stranski-Krastanov layer plus island growth [24].

2.2.3 Structure Zone Models

The microstructure of a film, as one can imagine, is one of the most influencing variables related to the properties of a thin film. Due to the non-equilibrium nature of most PVD-methods, unique coating-microstructures may be obtained. By control of the microstructure, properties of the film such as intrinsic stress, refractive index, electrical resistivity, etc., can be promoted. Therefore, it is useful to understand the dependence of film microstructure on the deposition parameters, which are generally depicted in so called *structure zone diagrams or -models (SZMs)* [2, 23, 28].

The first SZM was a three-zone model introduced by *Movchan* and *Demchishin* in 1969 (**Fig. 2.14 a**). They found – based on observations on thick films up to 2 mm – that the morphological structure of evaporated coatings can be related to a reduced temperature Ts/Tm (where Ts is the actual film temperature during deposition and Tm is its melting temperature, both in K) [31]. In 1977 *Thornton* adapted this SZM by introducing additionally to the homologous temperature (Ts/Tm) an extra variable, i.e. the inert sputtering gas pressure (**Fig. 2.14 b**) [32]. The resulting SZM displays 4 zones (1, 2,3, T). Gas pressure affects the formation of deposited films via various indirect mechanisms. For example, by increasing the pressure the mean free path for collisions between sputtered atoms and working gas decreases and hence the oblique deposition flux increases resulting in a lower kinetic energy of the vapor species and thus in a more open zone 1 structure. Additionally, increased pressure has been suggested to lower the adatom mobility. On the other hand, a low pressure leads to denser films caused by the increased energetic particle bombardment [33].

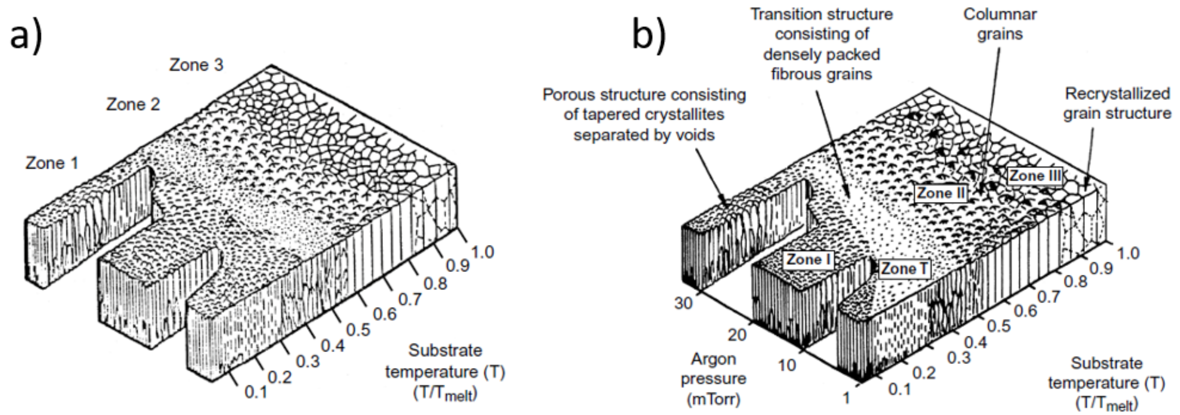

Figure 2.14: Structure zone models (SZMs) of vacuum evaporated condensates. SZM for thick evaporated films adapted from Movchan and Demchishin (1969). **b)** SZM for sputter-deposited films adapted from Thornton (1977) [2].

The microstructure in *Zone 1* ($T_s/T_m < 0.3$) is characterized by tapered columns with a domelike top. The reason for this is the negligible diffusion of the trapped atoms leading to shadowing effects. Hence the major amount of the sputtered flux is deposited at elevated peaks of the coating and little material reaches the valleys in between. Zone 1 microstructure shows a high dislocation density and high porosity. The transition *Zone T* is in between Zone 1 and Zone 2. A denser small grained structure is formed. Compared to the bordering zone structures, Zone T films show a smoother surface. High energy neutrals arising from the sputtering target at low gas pressure bombard the surface. This leads to erosion of the peaks and to filling of the valleys to some amount. They are typically hard, show a high dislocation density and provide high strength and low ductility. The start of *Zone 2* ($0.3 < T_s/T_m < 0.5$) is determined by the activation of grain boundary migration. The growth process is dominated by adatom surface diffusion and leads to a densification of the intracolumnar boundaries. However, the basic columnar morphology remains, but the grain size increases. Zone 2 films are hard but show a low ductility. Above a homologous temperature of 0.5, *Zone 3* structures appear. Here bulk diffusion allows recrystallisation, grain growth and densification. The structure shows a highly modified columnar morphology with large equiaxed grains being single crystals and appears with a bright film surface. Zone 3 films provide a soft recrystallized grain structure with a low dislocation density [2, 23, 24, 26].

In order to point out the influence of some basic growth conditions, four different growth structures have been established, suspecting extreme cases of surface diffusion, condensation coefficients and nucleation. **Figure 2.15 (a)** shows the case of zero surface diffusion and a unity condensation coefficient. Initial nuclei have a spherical shape and a flux mostly normal to the substrate surface will result in a dense columnar coating structure. This is the structure found

generally in Zone T. Conversely, zero surface diffusion in combination with a condensation coefficient dependent on the crystallographic surface leads to a growth of specific nuclei (**Fig. 2.15 (b)**). Zone 1 structures show this open and rough morphology. Infinite surface diffusion appearing with a flux perpendicular to the surface results in growth of all crystals with the same rate to form a dense film with a smooth but though facetted surface. This is the case when the substrate temperature T_s is rather high and figures out to be the common Zone 2 structure (**Fig. 2.15 (c)**). The fourth structure (**Fig. 2.15 (d)**) is formed when infinite surface diffusion and periodic nucleation is given. Reasons for periodic nucleation may be impurities or may be caused by an increased number of impinging particles [32, 34].

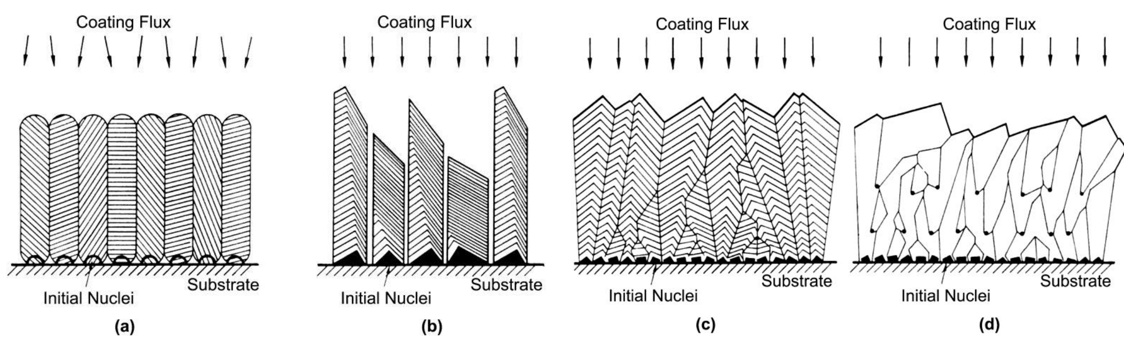

Figure 2.15: Two-dimensional growth structures constructed for several extreme cases of adatom surface diffusion. **(a)** Zero surface diffusion, unity condensation coefficient. **(b)** Zero surface diffusion, condensation coefficient dependent on crystallographic surface. **(c)** Infinite surface diffusion. **(d)** Infinite surface diffusion with periodic renucleation [32].

2.3 Nano Cluster Deposition via Gas Phase Synthesis

Like already mentioned in section **2.1.4.2**, nano clusters have been investigated as functional modules for gas sensors but further also for many other technological applications. In general, there are two categories to classify the formation of nano clusters into: a) *top-down* methods and b) *bottom-up* methods. Whereas the principle of top-down formation of nano clusters is the systematic removing of material from a substrate leaving the nano structures, in bottom-up nano fabrication nano clusters are formed by assembly from smaller structures [35]. Considering the functionalization on gas sensing surfaces with nano clusters in gas sensors, the method to focus on is the bottom-up method *gas-phase synthesis,* which allows depositing nano clusters on a sensor surface without affecting too much the sensing surface or other functional structures existing in a gas sensing device. An aimed etching, e.g. of a certain component of a previously deposited film in order to produce nano clusters, may also affect other device components.

In gas-phase synthesis, nano clusters are made by building them from individual atoms or molecules up to the desired size. Cluster embryos are formed either by physical means such as condensation of a supersaturated vapor or by chemical reaction of gaseous precursors. Depending on process parameters temperature, pressure and embryo concentration, these clusters continue to grow to larger entities by coagulation and coalescence and/or surface growth [36]. As one can now conclude from the dependence of these various parameters, gas-phase synthesis allows to handle the characteristics of the deposited particles. A schematic of a magnetron sputter inert gas condensation nano cluster deposition system is shown in **Fig. 2.16 a)**, whereas the dependence of deposition rate of Pt-nano clusters on pressure in the aggregation chamber and different magnetron currents is plotted in **Fig. 2.16 b)**.

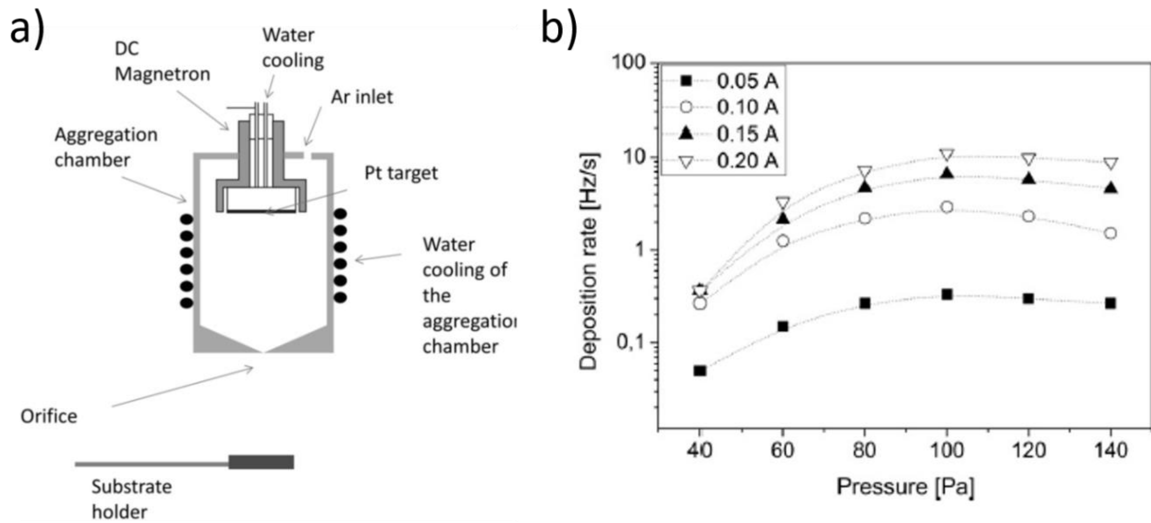

Figure 2.16: **a)** Schematics of a magnetron sputter inert gas condensation nano clusters deposition system. **b)** Deposition rate of Pt nano clusters in dependence on pressure in the aggregation chamber measured for different magnetron currents [37].

2.3.1 Particle Formation

According to WEGNER et al. [36], formation of particles in the gas phase takes place either by homogeneous nucleation or by coagulation (collision) processes. The starting material is usually vaporized from a liquid source or a sputter target into a low-density inert gas. Commonly an inert gas is used as condensation gas. In magnetron sputter inert gas condensation systems often a mixture of argon (for sputtering) and helium (for condensation) is used [38]. The metal atoms effused from the source collide with gas atoms, which brings along a fast-exponential cooling and therefore leads to a supersaturation followed by homogeneous nucleation of the metal. This early stage is necessary to reach a suitable temperature that allows bond formation. The critical diameter d_{crit} is given from simple equilibrium thermodynamics:

$$d_{crit} = 4\gamma \left[\rho RT \ln\left({}^{p_v}/_{P_0}\right)\right]^{-1} \tag{2}$$

There, γ is the surface tension, ρ is the density, R is the gas constant for the metal vapor at absolute temperature T and p_v/p_0 represents the supersaturation ratio, i.e. the true vapor pressure (determined by the source temperature T_s) divided by the equilibrium vapor pressure for the actual pressure. Consequently, due to rapid cooling of the metal vapor, d_{crit} is expected to be extremely small (**Fig. 2.17**) [36, 39].

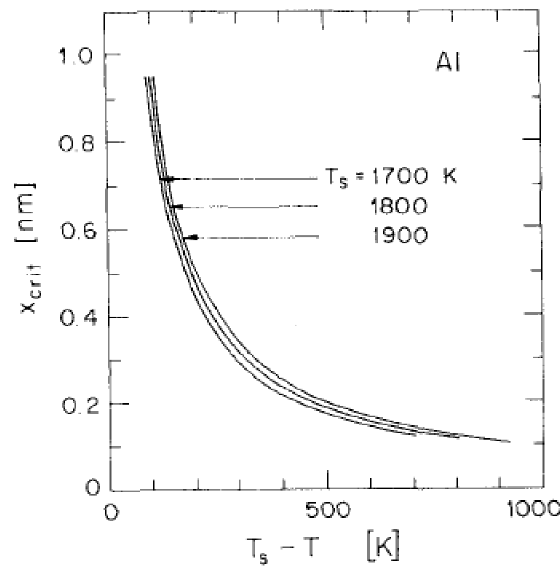

Figure 2.17: Critical diameter of nano clusters versus temperature for three values of the source temperature, Ts. The lines represent a calculation for Al using Eq. (2) [39].

2.3.2 Particle Growth

The further growth of the particle embryos takes either place via surface growth or via coagulation. Surface growth can be split up in two steps: first step is the transport of a molecule or atom to the surface of an already-formed particle and second step is the addition of the molecule or atom to the preexisting particle involving a chemical reaction or a phase change at the particle surface. Especially in the primer stages of particle formation from supersaturated vapor, surface growth is strongly contributing since initially formed clusters act as condensation seeds. By controlling the supersaturation at a low level, particle nucleation can be slowed down, while the rate of surface growth by vapor deposition can be increased [40]. In systems with chemical reactions, atoms or molecules transported to the particle surface do either react with the particle changing its chemistry or react at the particle surface with other gaseous species present in the system. The reaction product is then deposited on the particles surface. Generally, surface growth contributes to the whole particle growth when vapor or gas molecules are available in sufficient quantity [36].
Coagulation describes particle-particle collisions mainly due to Brownian motion but also due to other mechanisms like shear or electrostatic forces. In principle, coagulation is achieved by the coalescence of two or more nano clusters. Full coalescence (resulting in spherical product particles) takes only place at sufficiently high temperature, when particles are present as low viscosity liquid droplets. In contrast, at lower temperatures the process can be described as a

sintering process of two or more particles sticking together. This sintering leads to a formation of agglomerates with usually non spherical product particles [3, 36, 38, 39].

3 Experimental

3.1 Coating Deposition

3.1.1 Deposition System

All tin oxide coatings for this work were deposited with a DC unbalanced magnetron sputter device at the Montanuniversität Leoben. The system is custom-made by the Chair of Functional Materials and Materials Systems. It consists of a steel chamber housing three unbalanced magnetrons (AJA A320 XP) with permanent magnets and manual shutter systems, focused on a rotating substrate holder. A Helmholtz-coil system allows to superpose the permanent magnets field with an additional magnetic field. The chamber is evacuated by a sliding vane rotary pump (Pfeiffer DUO20) and a turbo molecular pump (Pfeiffer TMH 521) in series to a pressure ≤ 10^{-3} Pa. In order to deposit multicomponent films, up to three two-inch diameter targets either in reactive or non-reactive mode can be used. Angle and distance between the targets and substrate holder can be varied. The rotating substrate holder can be heated up to 800 °C by two halogen lamps. The heating is controlled by an AJA SHQ-15A controlling system using an Ogden ETR 9300 regulator. The deposition system has three MKS ENI RPG-50 power supplies of which two run the magnetrons (one controls one magnetron and the other one two magnetrons via a switchbox) and the third one is for bias voltage supply. The chamber has three gas inlets. Mass flow is steered by three Mykrolis mass flow controllers. Standard configuration is a gas flow from 0 – 400 sccm for argon and 0 – 40 sccm for nitrogen and oxygen. The pressure is measured with a PKR 251 Compact Full Range Gauge by Pfeiffer Vacuum Technik. Pressure of the whole operating range from 10^{-5} Pa up to 10^{3} Pa can be measured and displayed. Accuracy is at ca. ± 30 % with a reproducibility of ± 5 %. **Fig. 3.1** shows a schematic depiction of the vacuum chamber of the custom-made sputter system “Josefine II”.

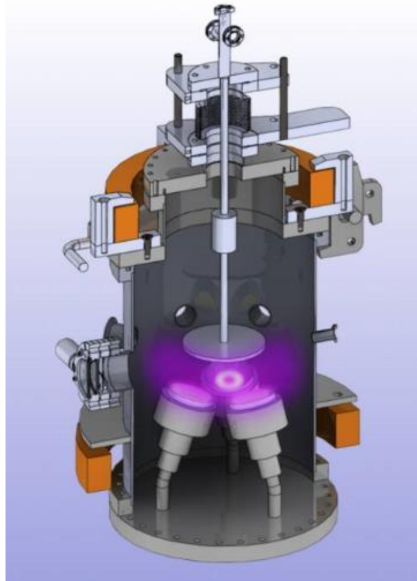

Figure 3.1: Schematic depiction of the vacuum chamber of "Josefine II".

3.1.2 Target, Substrate Materials and Working Gases

For the deposition of the SnO_X films, a tin target with a purity of 99.99 % and dimension of Ø 50.8 mm × 6 mm was used.

The coatings were deposited on silicon wafers in (100) orientation and glass plates. Both substrates were cut into pieces of ca. 6.5 mm × 20.5 mm. The silicon substrates were intended for elastic recoil detection analysis, X-ray diffraction analysis, focused ion beam microscopy, Raman spectroscopy, optical profilometry and elastic recoil detection analysis. The glass substrates were intended for electrical resistance measurements and for Raman spectroscopy.

For reactive sputter deposition, a mixture of argon and oxygen working gas, both with a purity of 99.999 %, were used.

3.1.3 Deposition Procedure

Before deposition, the substrate samples were cleaned in supersonic baths in ethanol for 10 min. After mounting on the substrate holder, the chamber was evacuated to a pressure below 1×10^{-5} Pa and heated to the desired temperature before the deposition procedure. As a next step of the deposition procedure the substrates were ion etched for 10 seconds, before the actual deposition started. The total pressure in the vacuum chamber during the deposition was set at 0.5 Pa. In order to get tin oxide films with different oxygen contents, the relative

oxygen partial pressure $p_{O2}/(p_{O2}+p_{Ar})$ was adjusted by varying the gas flows of oxygen and argon. Films with $p_{O2}/(p_{O2}+p_{Ar})$ ratios of 50, 60, 70, 75, 80, 85 and 90 % were deposited. The deposition temperatures were room temperature, 100 °C, 150 °C and 200 °C. Immediately after substrate etching, the deposition of the films started. The target power during the procedure was kept constant at 50 W. In order to obtain a film thickness above 100 nm, a deposition time of 7 minutes and 30 seconds was chosen. **Table 3.1** provides an overview on the used deposition parameters.

Table 3.1 Overview on the used parameters to deposit SnO_X films.

$p_{O2}/(p_{O2}+p_{Ar})$ [%]	Total Pressure [mbar]	Ar Flow [sccm]	O_2 Flow [sccm]	P [W]	U [V]	I [A]
50	4×10^{-3}	15	6	50	432	0.11
60	4.39×10^{-3}	12	6.5	50	399.7	0.12
70	4.02×10^{-3}	10	7.5	50	401.3	0.12
75	5×10^{-3}	8	8	50	427	0.11
80	3.65×10^{-3}	7	8.6	50	417.9	0.12
85	3.4×10^{-3}	6	9	50	436.4	0.11
90	3.4×10^{-3}	5	9.4	50	438.2	0.11

After deposition, some selected samples were annealed in air atmosphere for 30 min. at 500 °C and 600 °C for 30 min, respectively. The used furnace was a Nabertherm N 11/HR.

3.2 Coating Characterization

3.2.1 X-Ray Diffraction Analysis

X-ray diffraction (XRD) has established as a non-destructive characterization technique for phase determination in crystalline materials. Moreover, structural properties such as texture, grain size or residual stress of a coating can be analysed.

Under electromagnetic irradiation with a wavelength in the order of magnitude of the lattice dimension, a crystalline material shows a characteristic diffraction pattern [41]. Bragg's law correlates the lattice planes spacing d_{hkl} where h, k, l indicate the Miller indices, the wavelength of $\lambda_{X\text{-}ray}$ of the used radiation and the scattering angle θ and can be written as:

$$d_{hkl} = \frac{n\lambda_{X-ray}}{2\sin\theta}, \quad (3)$$

with *n* being an integer. By comparing the obtained diffraction patterns with the line positions 2θ and relative line intensities of standards, e.g. from the International Centre for Diffraction Data (ICDD), the present phases can be identified. Alternatively, the diffractogram may be compared with a calculated one, derived from some hypothetical model of the crystal structure [41].

The X-ray diffraction measurements were carried out with a Bruker-AXS D8 Advance diffractometer using Cu K_{α} radiation. A Goebel mirror was used to achieve a parallel and monochromatic radiation. The measurements were performed with Bragg-Brentano scanning geometry and a 2θ angle between 20° and 60°. A Sol-X detector was used. The operating parameters in **Tab. 3.2** were kept constant for all measurements.

Table 3.2 Parameters for XRD-measurements.

λ Cu K_{α} [Å]	High Voltage [kV]	Tube Current [mA]	Step Time [s]	Step Size 2θ [°]
1.54056	40	40	1.2	0.2

3.2.2 Raman Spectroscopy

Raman spectroscopy is a vibrational spectroscopy method, which is used to study a wide range of materials and sample types. Vibrational spectroscopy has a very broad range of applications and provides a host of important and challenging analytical problems. Samples may be either in bulk or in microscopic amounts over a wide range of temperatures and physical states (e.g. gases, liquids, powders, fibres, films, etc.) [42].

The principle of Raman spectroscopy is the observation of inelastically scattered photons from a monochromatic light source such as UV-lasers, lasers in the spectral region of visible light as well as the near IR-spectral region. When the photons interact with phonons or molecular vibrations, their energy may be either shifted up or shifted down. These energy shifts are the so-called *Raman shifts.* The light scattered photons include mostly the dominant Rayleigh and the very small amount of Raman scattered light [43]. The Rayleigh and Raman processes are schematically depicted in **Fig. 3.2**.

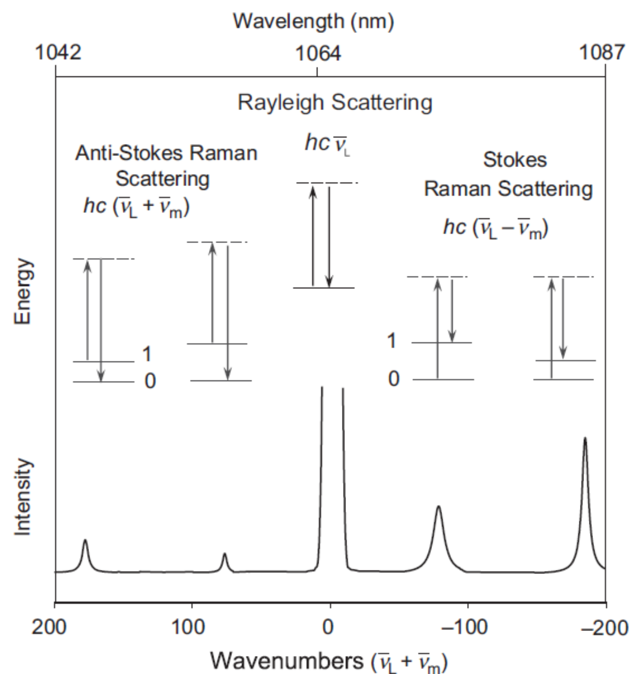

Figure 3.2: Schematic illustration of Rayleigh scattering as well as Stokes and anti-Stokes Raman scattering. The laser excitation frequency (ν_L, represented upward arrows) is much higher than the molecular vibration frequency (ν_m). The frequency of the scattered photons is represented by the downward arrows [42].

While no energy is lost in the elastic Rayleigh scattering, Raman scattering is an inelastic process and hence energy is changed. The scattering process involves momentaneous absorption from incident light by transition from the ground state into a virtual state. Then a new photon is created and scattered by transition from this virtual state either back into the ground state (Rayleigh scattering) or into the first excited state of the molecular vibration (Raman scattering). Since the energy of the first excited state of molecular vibration differs from the ground state, this is described as an inelastic scattering process [42].

Fig. 3.2 indicates that there are two types of Raman scattering: Stokes and anti-Stokes. Molecules initially in the ground vibrational state (indicated as 0) lead to Stokes Raman scattering $hc(\nu_L-\nu_m)$, while molecules initially in the excited vibrational state (indicated by 1) lead to anti-Stokes Raman scattering $hc(\nu_L+\nu_m)$. The intensity ratio of the Stokes relative to the anti-Stokes Raman bands is governed by the absolute temperature of the sample and the energy difference between the ground and excited vibrational states [42]. The observed intensity of Raman scattering I_R is typically ca. 10^{-6} that of the incident light used for strong Raman scattering and is much lower than the intensity of Rayleigh scattering (10^{-3}) and is given by:

$$I_R \propto \nu^4 I_0 N \left(\frac{\partial\alpha}{\partial Q}\right)^2 , \quad (4)$$

where I_0 is the incident laser intensity, N is the number of scattering molecules in a given state, ν is the frequency of the exciting laser, α is the polarizability of the molecules and Q is the vibrational amplitude. Eq. (4) indicates, that only molecular vibrations which cause a change in polarizability are Raman active:

$$\left(\frac{\partial_\alpha}{\partial Q}\right) \neq 0. \quad (5)$$

Raman vibrational bands are characterized by frequency (energy) intensity (polar character or polarizability) and band shape (environment of bonds). The frequencies of the molecular vibrations depend on the masses of the involved atoms, their geometric arrangement and the strength of their chemical bond, hence they provide information on molecular structure, dynamics and environment. Since the vibrational energy levels are unique to each molecule, the Raman spectrum provides a “finger print” of a particular molecule [42].

The measurements for this work were performed on a Horiba Yvon Labram 300 integrated Raman system coupled with an Olympus BX40 confocal microscope. The used excitation laser was an internal 100 mW Nd-YAG laser with a wavelength of 532.02 nm (green). For each measurement the acquisition time was 20 seconds and the number of accumulations was 3.

3.2.3 Elastic Recoil Detection Analysis

Since the practical properties of many materials depend on surface and near surface composition and the contaminants in these areas are light elements (i.e. oxygen, nitrogen, hydrogen and carbon), there is a need for an analytic probe that simultaneously and qualitatively records elemental profiles of all light elements. Compared to other quantitative analysis methods like Rutherford Backscattering Spectroscopy (RBS), which has limitations in mass resolution for heavy elements and poor sensitivity for light elements, Elastic Recoil Detection Analysis (ERDA) represents a very useful method to provide quantitative depth profiles of light and medium mass elements in virtually any material [44–46].

In ERDA a beam of positive ions coming from a Van de Graaff accelerator, a tandem or a cyclotron hits the solid sample in the near surface area. Most of the incident ions are simply elastically scattered, but some interact with isotopes of light elements in the sample, when the energy of an incident ion is high enough that a sample nucleus recoils from the surface. **Fig. 3.3** shows a sketch of the ERDA principle.

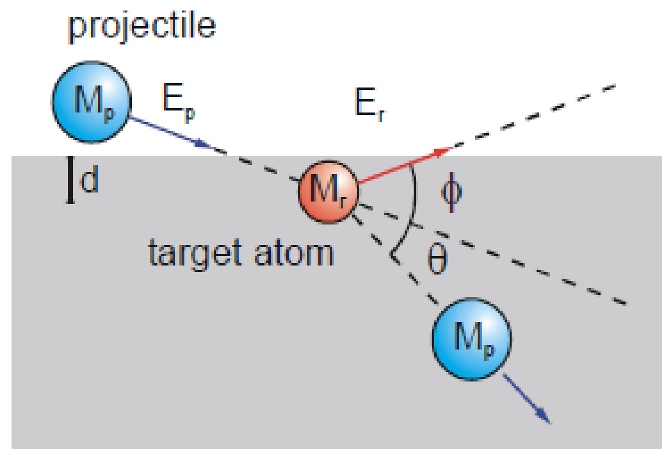

Figure 3.3: Sketch of the ERDA principle [47].

This elastic recoil process is simply describable using kinematic equations from the physics of elastic collisions [44]. The energy E_r of a recoiled atom of mass m_r at an angle Φ transferred by projectile ions of mass m_p and the energy E_p is given by:

$$E_r = \frac{4 m_p m_r}{(m_p + m_r)^2} E_p \cos^2(\Phi) \tag{6}$$

Eq. 6 can also be written as:

$$\frac{E_r}{m_r} = \frac{4\cos^2(\Phi)}{\left(1+\frac{m_r}{m_p}\right)^2} \frac{E_p}{m_p} \tag{7}$$

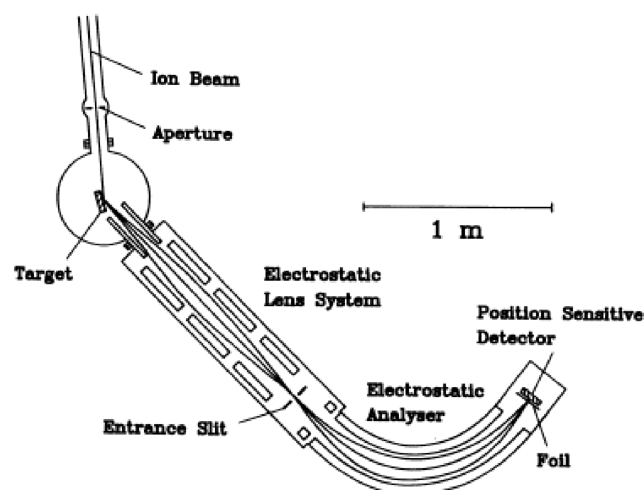

Figure 3.4: Sketch of an ERDA measurement system [48].

Figure 3.4 shows a sketch of an ERDA measurement system. Often in between the sample and the detector an absorber foil is placed, which due to the greater stopping power of materials with respect to high mass ions reduces the kinetic energy of the forward scattered He ions sufficiently, so that they do not overlap with the signals detected due to isotopes of e.g. hydrogen [46]. The energy of the detected particle is a simple function of mass and geometry (eq. (6)).
ERDA measurements were carried out at the Helmholtz-Center Dresden-Rossendorf using a 43 MeV Cl^{7+} ion beam. The angle between the sample normal and the incoming beam was 75° and the scattering angle was set to 30°. An area of about 2 × 2 mm^2 was analyzed. The recoil atoms and the scattered ions have been detected with a Bragg Ionization Chamber, which enables energy measurement and Z (atomic number) identification of the particles. H recoils have been detected with a separate solid-state detector at a scattering angle of 40°. This detector is preceded by a 25 µm Kapton foil, which stops scattered ions and heavy recoil ions. The spectra and the RBS (Cl scattering) were fitted simultaneously using the program NDF v9.6i [49].

3.2.4 Focused Ion Beam Investigation

Focused Ion Beam (FIB) is a technology often used in materials science for site specific analysis, sample ablation and deposition. FIB systems use a defined beam of (commonly Ga+) ions coming from a liquid metal ion source (LMIS), which interacts with a solid. At rather low beam currents FIBs are used for imaging, at high currents for milling, or local sputtering. Milling takes place as a result of physical sputtering and occurs as the result of a series of elastic collisions, where momentum is transferred from the incident ions to the sample atoms within a collision cascade region. Inelastic scattering events of ions can result in the production of phonons, plasmons (in metals) and the emission of secondary electrons (SE). The detection of latter is the standard mode for imaging in the FIB. However, secondary ions may also be detected and used for imaging [50]. **Figure 3.5** shows the ion-solid interactions occurring in a FIB system.

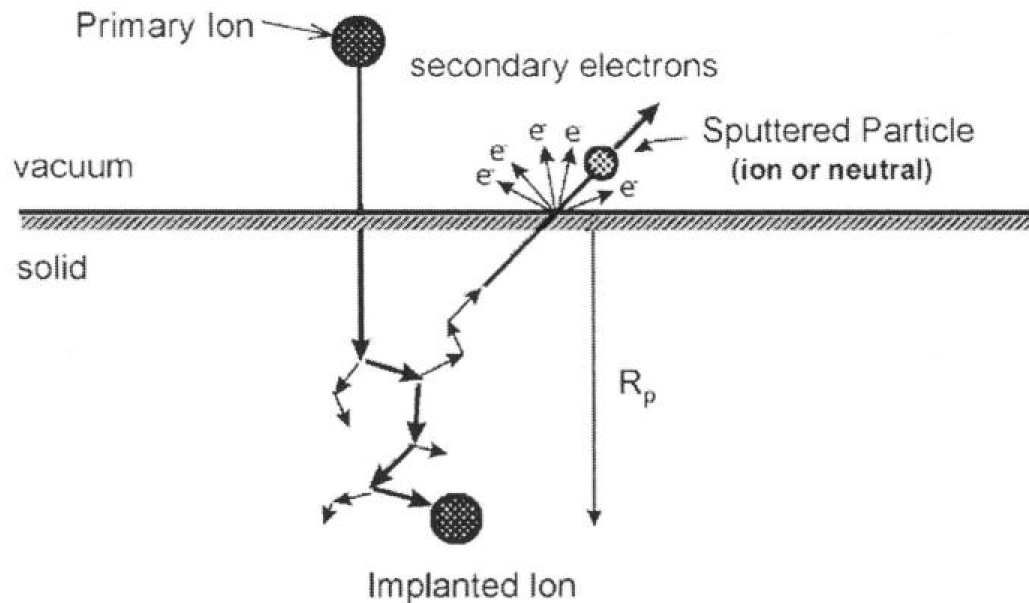

Figure 3.5: Schematic diagram of the sputtering process and ion-solid interactions [50].

In this work, the focused ion beam was used to cut into the thin film sample for investigation of the cross section of the films and for thickness measurements. The used FIB was an Orsay Physics Cobra Z-05.

3.2.5 Scanning Electron Microscopy

Scanning electron microscopy (SEM) was used to investigate the film surface and cross section morphology and measure the coating thickness of the FIB cut films.

The qualitative elemental composition of the cut coatings was measured by energy-dispersive X-ray (EDX) emission spectroscopy. In EDX, the sample surface is bombarded with electrons and characteristic X-ray beams which are specific for the elements hit by the electrons are emitted.

The measurements were performed on a Zeiss SMT Auriga SEM.

3.2.6 Four-Point Resistivity Measurement

The four-point resistivity measurement is a widely used method to determine the electrical resistivity of thin films. Four equidistant metal tips are brought to the film surface, where a known current flows between the two outer ones through the film. Between the inner two tips, the difference in potential is measured and according to Ohm´s law the electrical resistance of the film material may be determined. The measurement system used in this work was a Jandel Model RM2.

3.2.7 Atomic Force Microscopy

Atomic force microscopy (AFM) is a term used for microscopy methods, which use a force interaction of a so-called probe and the sample to visualize the surface. The probe scans the surface to investigate it step by step and collects measured data for each point. The resulting data is than analyzed and converted into a digital picture. The probe is mounted on a cantilever-type spring and deflected after approaching the sample. These deflections can be measured, and a topographic map of the samples' surface is obtained. The used microscope was a Semilab BRR 2770.

4 Results and Discussion

4.1 Film Surface Topography and Morphology

After FIB cutting into selected thin film samples , the surface topography and film morphology were investigated by SEM. **Figure 4.1** and **Figure 4.2** show representative scanning electron micrographs of the films deposited at 100 °C at a $p_{O2}/(p_{O2}+p_{Ar})$ of 60 % and 80 %, respectively, onto Si substrates both for the as deposited condition and after annealing for 30 min at 500 °C.

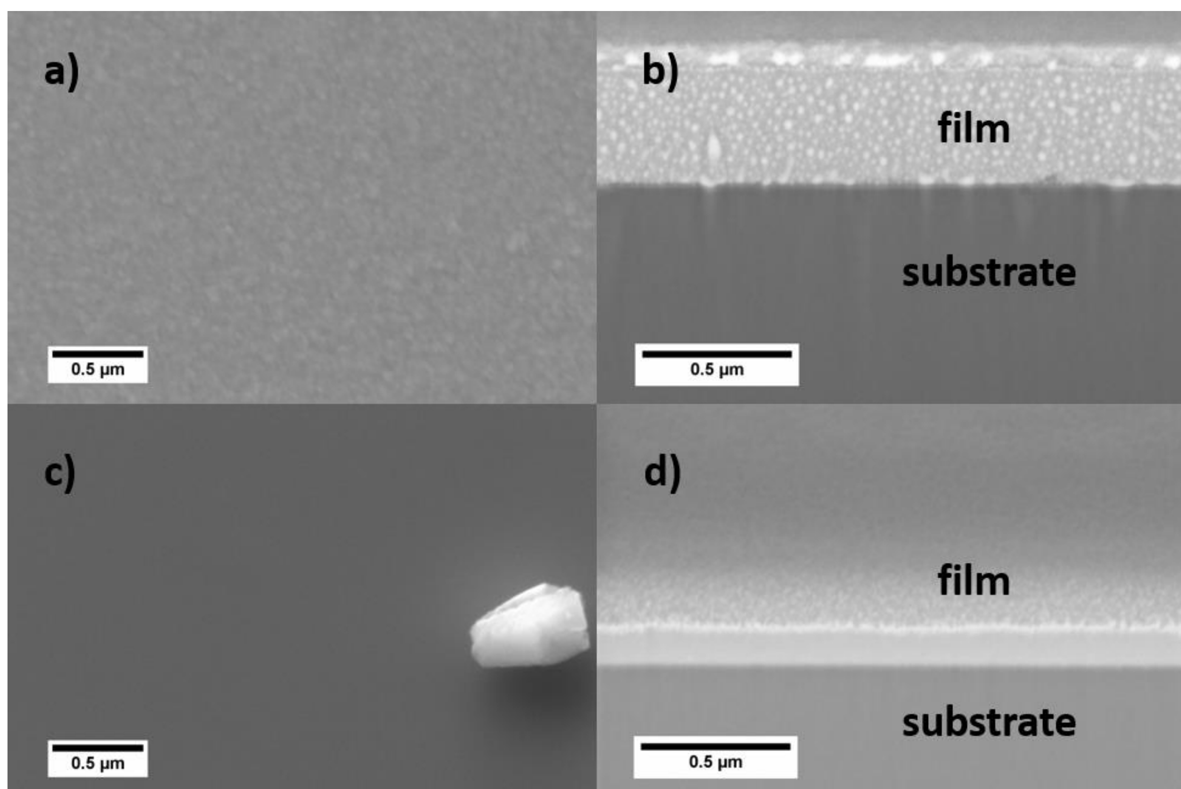

Figure 4.1: Secondary electron SEM images of surfaces and cross sections of tin oxide sputter deposited at 100 °C on Si substrates. **a)** surface and **b)** corresponding cross section of a film grown at $p_{O2}/(p_{O2}+p_{Ar})$ = 60 %. **c)** Surface and **d)** corresponding cross section of a film grown at $p_{O2}/(p_{O2}+p_{Ar})$ = 80 %.

Fig. 4.1 a) shows that the film deposited with an oxygen partial pressure $p_{O2}/(p_{O2}+p_{Ar})$ of 60 % is characterized by a smooth surface with low roughness, whereas for $p_{O2}/(p_{O2}+p_{Ar})$ = 80 % even a further smoothening was observed. The cross section of the film deposited with the

lower oxygen partial pressure (**Fig. 4.1 b)**) appears dense without any pores and holes and exhibits small bright particles embedded in a dark matrix, which could indicate the coexistence of crystalline and amorphous structures. The film deposited with $p_{O2}/(p_{O2}+p_{Ar})$ = 80 % (**Fig. 4.1 c)**) on the other hand appears also dense without discontinuities, but does not show bright spots as it was observed for the film deposited with $p_{O2}/(p_{O2}+p_{Ar})$ = 60%. The images indicate a good adhesion between the substrate and the coating layers without any cracks at the interface.

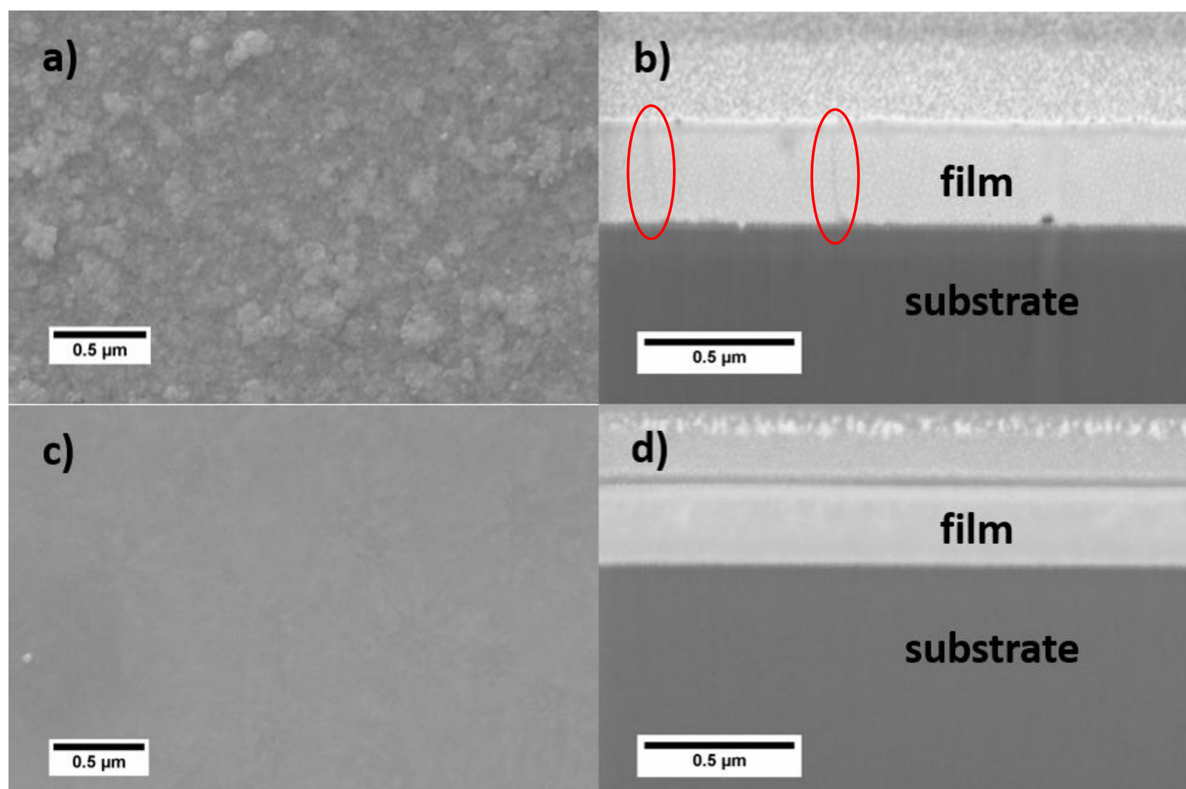

Figure 4.2: Secondary electron SEM images of surfaces and cross sections of tin oxide sputtered at 100 °C on Si substrates and annealed at 500 °C for 30 min. **a)** surface and **b)** corresponding cross section of a film grown at $p_{O2}/(p_{O2}+p_{Ar})$ = 60 % (existing cracks are highlighted by red ellipses). **c)** Surface and **d)** corresponding cross section of a film grown at $p_{O2}/(p_{O2}+p_{Ar})$ = 80 %.

After annealing the films for 30 min at 500 °C under air atmosphere, their surface topography as well as their cross-sectional morphology undergo changes. **Figures 4.2 a)** and **4.2 b)** evidence that the surface of the annealed film deposited at $p_{O2}/(p_{O2}+p_{Ar})$ = 60 % shows a significantly higher roughness than the as deposited samples (**Fig. 4.1 a) and b)**). The already existing bright grains in the as deposited samples seem to be coarsened at the surface and cracks are evident on the surface as well as in the cross section image (red ellipses in **Fig. 4.2**

b)). The cross section (**Fig. 4.2 b)**) indicates that the bright areas within the tin oxide film are smaller compared to the as deposited film (**Fig. 4.1 b)**). A thin slightly darker layer with a different morphology is visible at the original film surface, which could stem from a chemical reaction of the tin oxide with the atmospheric oxygen in the furnace at elevated temperatures. Comparing the as deposited and the annealed film grown at $p_{O2}/(p_{O2}+p_{Ar})$ = 80 % (**Fig. 4.2 c)** and **d)** and **Fig. 4.1 c)** and **d)**), changes of the film surface may be suspected. The annealed film's surface in **figure 4.2 c)** seems to be slightly roughened containing some bright fractions, whereas the as deposited films does not (**Fig. 4.2 c)**). On the other hand, the cross section of the annealed film (**Fig. 4.2 d)**) does not indicate significant changes compared to the as deposited film (**Fig. 4.1 d)**).

The results obtained within this thesis for the surface morphology agree with the work of *Guzmán-Caballero et al.* [51], who reported an evolution from rather granular surface topography towards a smooth and homogeneous surface with rising the oxygen partial pressure in the deposition chamber. The oxygen partial pressure range in their study was significantly lower (<20 %) compared to the oxygen partial pressure (>50 %) used for deposition in this work. According to them, the roughness of the film surfaces decreases due to a decrease of metallic tin in the films with increasing $p_{O2}/(p_{O2}+p_{Ar})$.

The film thickness was measured once via optical profilometry, which did not lead to clear results due to the fact, that most of the films are transparent and therefore difficult to evaluate. Nevertheless, the film thicknesses are in the range of 300 nm for films deposited with $p_{O2}/(p_{O2}+p_{Ar})$ = 60 % and 130 nm for the $p_{O2}/(p_{O2}+p_{Ar})$ = 80 % and 90 % films, respectively. The thickness of the selected films cut by FIB was measured on SEM micrographs from the cross section of the films. **Figure 4.3** illustrates two representative FIB cuts, where the film thickness was measured. The film thickness decreases with rising the $p_{O2}/(p_{O2}+p_{Ar})$ ratio. Reason for this phenomenon is presumed to be poisoning of the target [2] and therefore a lower deposition rate, which goes along with rising the oxygen partial pressure.

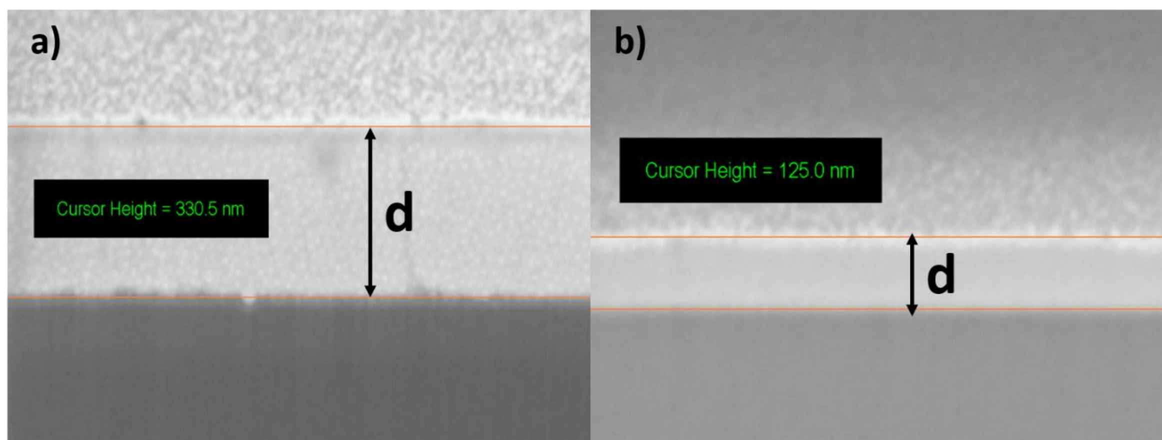

Figure 4.3: Measuring of the coating thickness on FIB cross sections for **a)** a $p_{O2}/(p_{O2}+p_{Ar})$ = 60 % and **b)** $p_{O2}/(p_{O2}+p_{Ar})$ = 80 % film (both annealed).

4.2 Elemental Composition

4.2.1 EDX

To obtain information about the chemical composition, the samples studied using SEM were further investigated by EDX. An example for the received elemental composition is shown in **Tab. 4.1**.

Table 4.1: Elemental composition of the $p_{O2}/(p_{O2}+p_{Ar})$ = 60 % film (thickness ca. 300 nm).

Element	Weight %	Atomic %
C	3.9	19.3
O	2.2	8.0
Ga	6.8	5.8
Si	15.8	33.0
Pt	7.7	2.3
Sn	63.6	31.6

The elements Ga, Pt and C stem from the preparation of the samples by FIB, where a Ga^+ ion beam was used. A Pt strip was applied to the surface as reference point for the FIB cutting. The C amount is rather high, and it is assumed to originate in sample exposure to the ambient and to sample, albeit the samples were cleaned in supersonic baths in ethanol for 10 minutes after the deposition. The other elements Sn, O and Si were expected to be found in the films,

where the Si substrate signal could not be avoided because of the low film thickness of 300 nm (see **Fig. 4.3 a)**). Although EDX provides a quantitative analysis of the investigated samples, it was only used to get a qualitative analysis due to the low film thickness and due to the fact, that oxygen is difficult to detect in EDX.

4.2.2 ERDA

For ERDA measurements, six selected samples were investigated. Five samples were reactively sputtered SnO_X films deposited with oxygen partial pressures of 60, 70, 80, 85 and 90 %. The last sample was a SnO_X film deposited via spray pyrolysis provided by the Materials Center Leoben (MCL), which was already successfully tested in a gas sensitivity measurement system. The results of the ERDA measurements for all samples are summarized in **Tab. 4.2**. The only film with carbon contamination is the sprayed layer, all sputtered samples do not show any trace of C. The contamination with hydrogen is between 0.40 and 0.95 at. %. No other elements have been detected. This low content of contamination elements (within the limits of detection) indicates a constant overall condition of the deposition system. The overall uncertainty is estimated to be about 1 at. % for Sn and O, 10 % (relative) for H and > 20 % (relative) for C. The measured depths of 281 nm to 392 nm does match with the film thickness.

Table 4.2 Average chemical composition of the SnO_X films as determined by ERDA.

$p_{O2}/(p_{O2}+p_{Ar})$ [%]	Sn [at. %]	O [at. %]	C [at. %]	H [at. %]	Depth [10^{15} at/cm²]	Depth [nm]
60	53.2	46.3	0	0.52	1754	392
70	46.7	52.9	0	0.40	1668	363
80	39.4	60.0	0	0.51	1490	316
85	37.3	62.1	0	0.60	1537	324
90	31.2	67.9	0	0.95	1362	281
sprayed	31.3	67.2	0.73	0.77	449	92

Figure 4.4 shows the depth profiles of the Sn-, O- and H-content for the sputtered samples and additionally the C- and Si-content for the sprayed layer, respectively. The depth profiles depicted in the graphs are directly based on the measured spectra. Therefore, they are convoluted with the system resolution and physical effects like straggling, meaning the actual sample composition can slightly different. The Si profile is not shown because of low statistics and low energy tailing of the Sn peak (Cl scattering), except for the sample of the spray pyrolysis film (**Fig. 4.4 f)**), where the SnO_X film is thin enough not to have this problem. Near

the film/substrate interface, the sputtered films show an increased Sn and a reduced O content in their depth profiles. This phenomenon is probably caused by drastic changes in stopping power between the adjacent layers. The H spectrum for the $p_{O2}/(p_{O2}+p_{Ar})$ = 60 % film shows more H in the second half of the layer (towards the interface). For $p_{O2}/(p_{O2}+p_{Ar})$ = 70 %, there is more H near the surface. For the other samples, the spectrum is uniform.

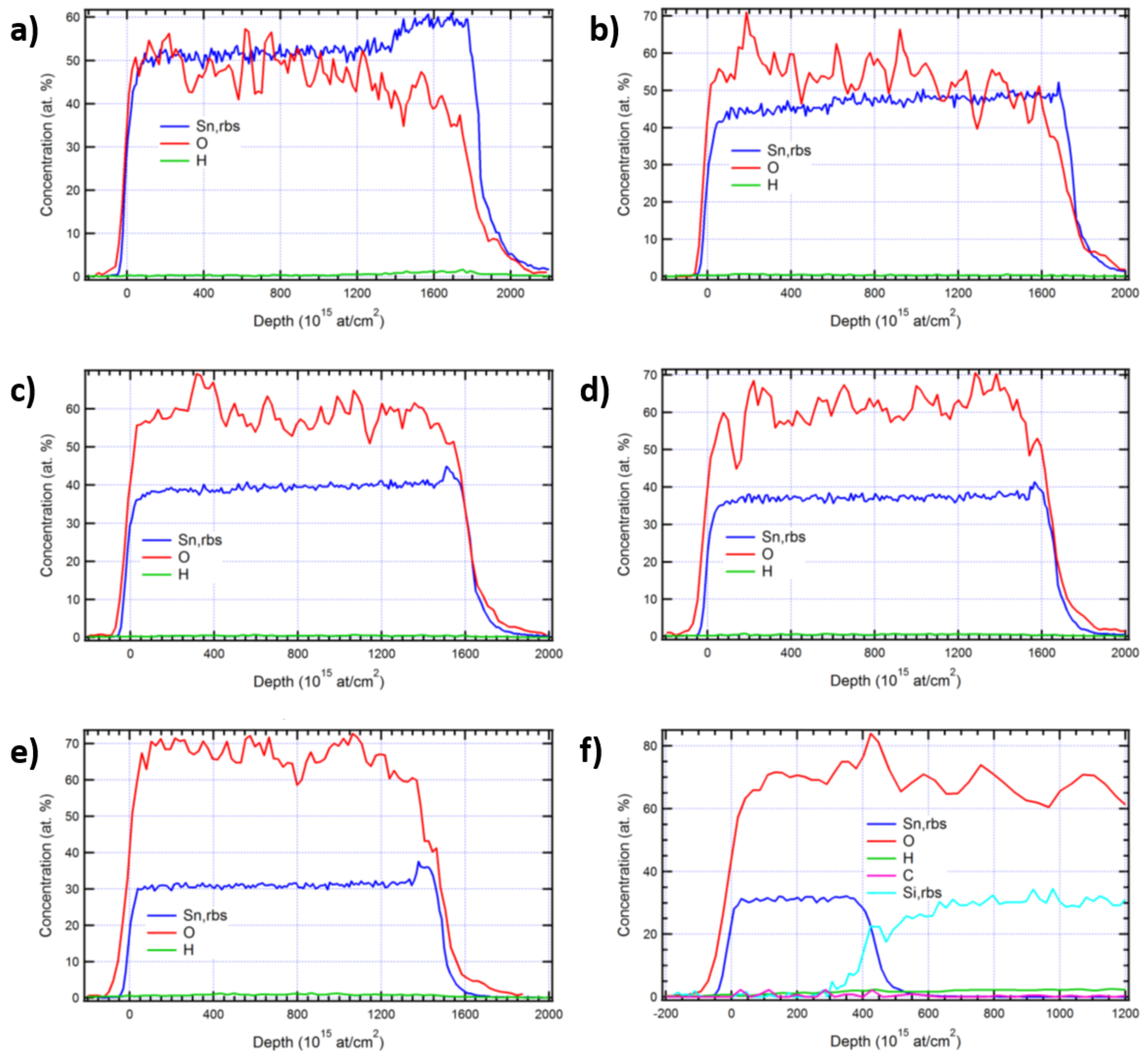

Figure 4.4: Depth profiles of the different elements for the deposited SnO_x films on Su substrates. Sputter deposited films with **a)** $p_{O2}/(p_{O2}+p_{Ar})$ = 60%, **b)** $p_{O2}/(p_{O2}+p_{Ar})$ = 70 %, **c)** $p_{O2}/(p_{O2}+p_{Ar})$ = 80 %, **d)** $p_{O2}/(p_{O2}+p_{Ar})$ = 85 %, **e)** $p_{O2}/(p_{O2}+p_{Ar})$ = 90 % and **f)** SnO_x film deposited via spray pyrolysis.

Comparing the results from EDX and ERDA measurements it can be concluded, that the high C-content determined by EDX is related to surface contamination of the samples -. ERDA

results show clearly that the films have been deposited under constant conditions in a clean environment. In the sputtered films, just H-contamination is notable, however, there is no obvious trend between $p_{O2}/(p_{O2}+p_{Ar})$ and H-contamination . The $p_{O2}/(p_{O2}+p_{Ar})$ = 90 % film shows a slightly higher H-content than the other films, however, the H content does not vary significantly. Regarding the Sn- and O-contents of the $p_{O2}/(p_{O2}+p_{Ar})$ = 60 % and 70 % films, one can roughly estimate non-stoichiometric compounds $SnO_{0.93}$ and $SnO_{1.06}$, respectively. The stoichiometry shifts to $SnO_{2.06}$ for the film deposited with $p_{O2}/(p_{O2}+p_{Ar})$ = 90 %, which is nearly the same as for the film deposited via spray pyrolysis. The latter has been shown to be promising for gas sensing applications in former experiments of the MCL. To summarize, it can be concluded that it is possible to synthesize films via reactive magnetron sputtering with chemical compositions similar wo those derived by spray pyrolysis.

4.3 Film Structure and Phase Composition

4.3.1 X-Ray Diffraction

The XRD investigations were performed on the tin oxide films deposited on Si (100) single crystal substrates in Bragg-Brentano θ-θ mode. The collected data has then been compared to reference diffraction data from Sn (ICDD card no. 00-005-0390), SnO (01-072-1012) and SnO_2 (01-075-9497_red & 01-078-1063_blue).

At room temperature, seven tin oxide films with different $p_{O2}/(p_{O2}+p_{Ar})$ ratios ranging from 50 up to 90 % were deposited and subsequently annealed at 500 °C for 30 min.

Figure 4.5: X-ray diffractograms of the tin oxide films sputter deposited at room temperature on Si substrates, for the as deposited and annealed (500°C/30 min) conditions.

Figure 4.5 evidences that nearly all the films in the as deposited condition have an amorphous structure, except for the film grown at $p_{O2}/(p_{O2}+p_{Ar})$ = 50% showing a wide peak at 30.6 ° which is assumed to correspond to metallic (100) oriented Sn grains. This is related to insufficient supply of oxygen, in order to form tin oxide. For the annealed films, the diffractograms show several peaks which indicate a crystalline fraction corresponding to SnO and SnO_2 grains with different orientations. Obviously, annealing in an oxidizing atmosphere results in formation of crystalline SnO_X phases in the films, while no metallic tin is found in the film after annealing – here the peak corresponding to pure tin in the $p_{O2}/(p_{O2}+p_{Ar})$ = 50 % disappears after the heat treatment. The patterns of the films with an oxygen partial pressure of 70 % and 75 % are

unchanged by annealing. It seems that an O content closer to full stoichiometry of the SnO and the SnO_2 phase (see **Tab. 4.2**) enhances the thermal stability of the films.

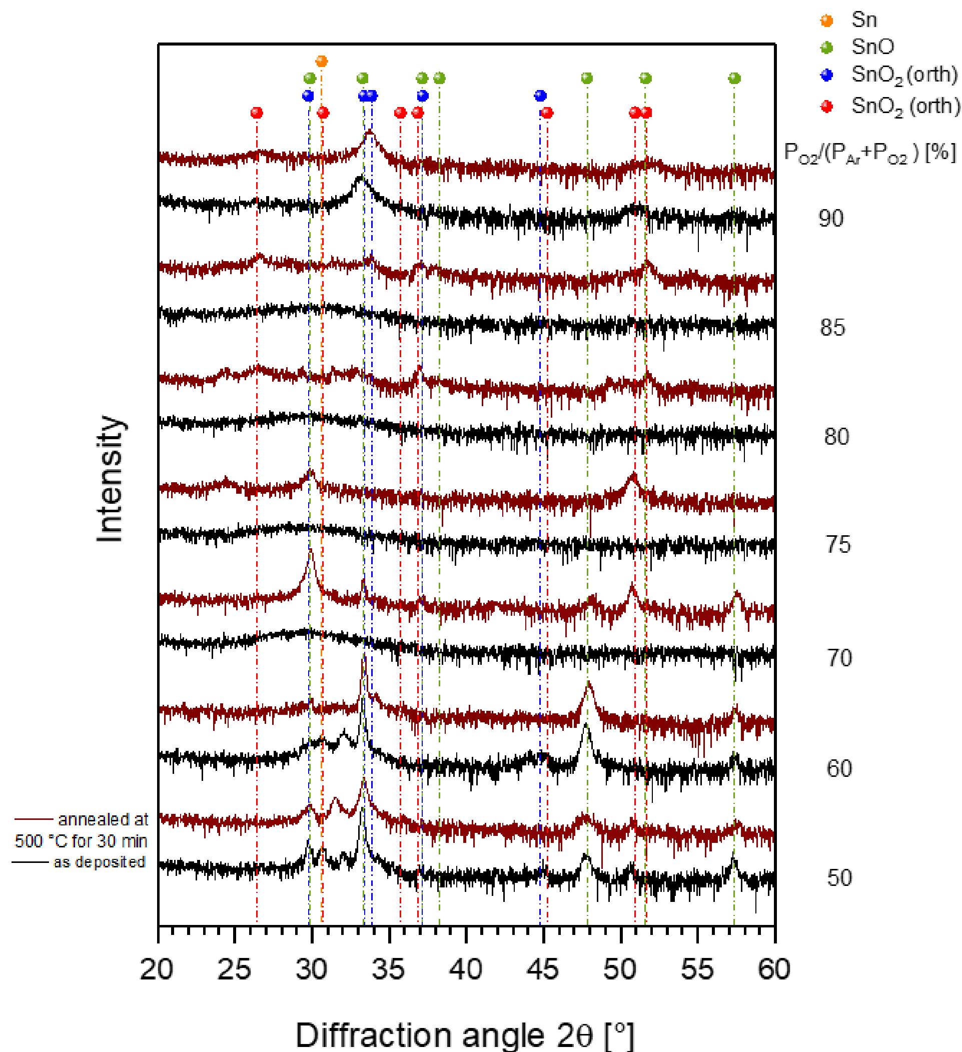

Figure 4.6: X-ray diffractograms of the tin oxide films sputter deposited at 100 °C on Si substrates, for the as deposited and annealed (500°C/30 min) conditions.

Additional films with the same oxygen partial pressures as described above were deposited at 100 °C and afterwards investigated by XRD. The X-ray diffractograms presented in **Fig. 4.6** confirm the speculations about the coexistence of crystalline and amorphous phases inferred from the SEM micrographs of the selected samples presented in section **4.1**. It is clearly visible, that the diffractograms of the films with $p_{O2}/(p_{O2}+p_{Ar})$ = 50 % and 60 % show unambiguous sharp peaks indicating the existence of crystalline tin oxides in the coatings. The peak at 33.3 ° is assumed to originate from crystalline SnO (ICDD: 33.292 °) in the films, which agrees well

to the observed stoichiometry (see **Tab. 4.2**). Also, the annealed $p_{O2}/(p_{O2}+p_{Ar})$ = 70 % film exhibits that peak. The diffractograms of the as deposited films in **Fig. 4.6** for an oxygen partial pressure of 70, 75, 80 and 85 % indicate a mostly amorphous structure. Here annealing of the samples leads to crystallisation of the films and the appearance of peaks in the diffractograms. The $p_{O2}/(p_{O2}+p_{Ar})$ = 90 % film has a peak at about 33.5 °, which due to the high oxygen partial pressure and the observed chemical composition (see Tab. 4.2) is referred to the existence of crystalline SnO_2. The impact of annealing on the films is that amorphous structure starts crystallizing with formation of tin oxides. In the films deposited with a lower amount of oxygen in the chamber, the peak corresponding to pure tin disappears after the heat treatment.

To illuminate the effect of different deposition temperatures on phase formation within the deposited SnO_X films, additional films were grown at room temperature, 100, 150 and 200 °C for $p_{O2}/(p_{O2}+p_{Ar})$ = 60 % and 80 %, respectively. The films were annealed for 30 min at two different temperatures (500 °C, 600 °C) and investigated by XRD to investigate the thermal stability and eventual phase changes during exposure to elevated temperatures (**Fig. 4.7**).

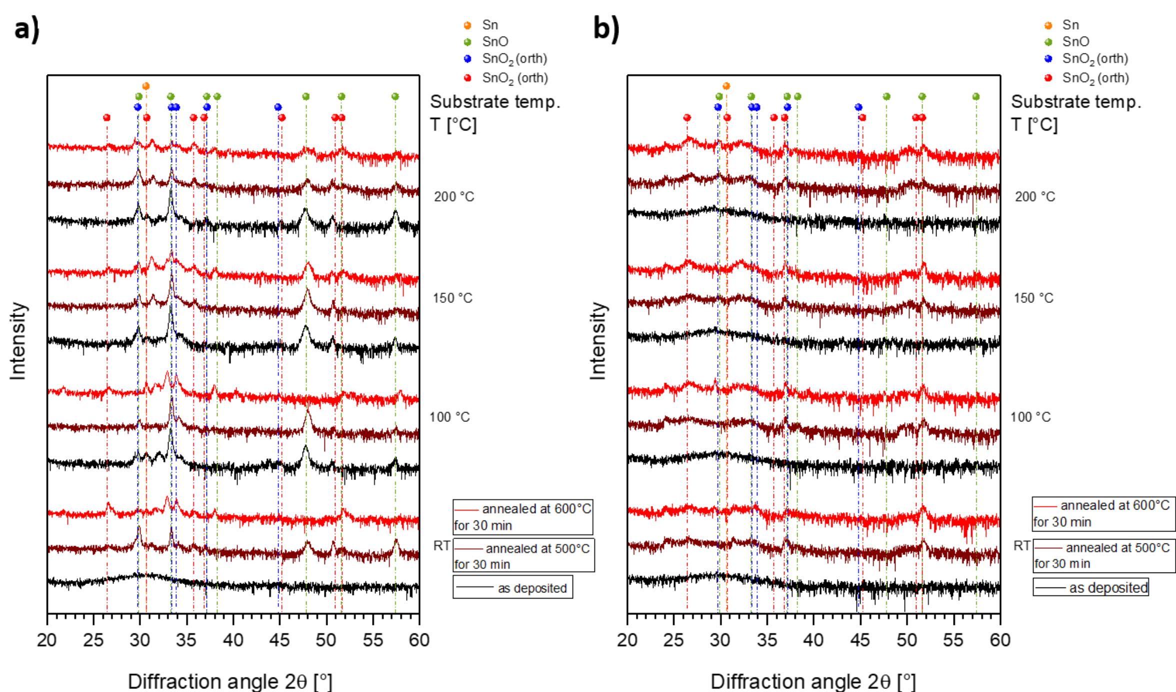

Figure 4.7: X-ray diffractograms of the tin oxide films sputter deposited on Si substrates at room temperature, 100, 150 and 200 °C, for the as deposited and annealed (500°C/30 min and 600°C/30 min) conditions. **a)** a $p_{O2}/(p_{O2}+p_{Ar})$ = 60 % and **b)** a $p_{O2}/(p_{O2}+p_{Ar})$ = 80 %.

The films deposited with an oxygen partial pressure of 60 % clearly show diffraction peaks when being synthesized at temperatures above 100 °C. The films with an oxygen partial pressure of 80 % seem to be amorphous independent of the substrate temperature. The effect of annealing is the same as described in the paragraphs above. No significant changes are observed due to the increase of the annealing temperature from 500 to 600 °C except for the 60 % film synthesized at room temperature and 100 °C (**Fig. 4.7 a)**). The latter, shows some changes which are obvious when comparing the patterns for annealing at 500 °C (brown graphs) and 600 °C (red graphs). The peaks at 29.86, 33.292 and 47.996 ° corresponding to SnO either do not exist in the red graphs or are at least less evident.

For an oxygen partial pressure up to 60 %, the X-ray diffractograms reveal that crystalline SnO_X and metallic Sn fractions are formed within the films, albeit for this purpose an elevated processing temperature is necessary. By further increase of the O_2 partial pressure, the diffractograms indicate an amorphous layer structure. The results obtained in this work partially agree with other studies found in literature [52–54], which report an amorphization of reactively sputter deposited metal oxides when the partial pressure of oxygen is increased above a certain value. *Luo et al.* [54] found, that at $p_{O2}/(p_{O2}+p_{Ar}) \leq 9.9$ % SnO_X films are dominated by a polycrystalline SnO phase, whereas an amorphous SnO_2 phase is formed at $p_{O2}/(p_{O2}+p_{Ar}) \geq 12.3$ %. The polycrystalline to amorphous film structure transition was ascribed to the enhanced crystallization temperature due to the perturbed structural disorder by incorporating Sn^{4+} into the SnO matrix [54]. It is noteworthy to mention that the oxygen partial pressure in this work was much higher than 12.3 %. In fact, it was possible to deposit tin oxide films with a $p_{O2}/(p_{O2}+p_{Ar}) = 60$ % at 100, 150 and 200 °C with crystalline fractions of SnO, SnO_2 and metallic tin, as evidenced by the XRD patterns in **Fig. 4.7 a)**. Implementing the conclusions from the ERDA measurements, the peaks corresponding to SnO and SnO_2 are referred to SnO for $p_{O2}/(p_{O2}+p_{Ar}) \leq 70$ % and to SnO_2 for $p_{O2}/(p_{O2}+p_{Ar}) \geq 85$ %.

4.3.2 Raman Spectroscopy

Raman spectroscopy measurements were performed on selected SnO_X films deposited at Si substrates using various $p_{O2}/(p_{O2}+p_{Ar})$ ratios. For most of the films it was not possible to receive conclusive Raman spectra, so the focus was laid on the films deposited with $p_{O2}/(p_{O2}+p_{Ar}) = 60$ % at different temperatures, for which conclusive results were received. The results were compared to reference spectra found in literature [53].

Figure 4.8 shows the Raman spectra for the $p_{O2}/(p_{O2}+p_{Ar})$ = 60 % films deposited at room temperature, 100, 150 and 200 °C. All the films are characterized by two significant peaks at 110 cm^{-1} and 210 cm^{-1}, which are related to SnO. Also visible are some smaller peaks below 100 cm^{-1}, which can be attributed to the existence of Sn_2O_3 and Sn_3O_4 phases in the films [53].

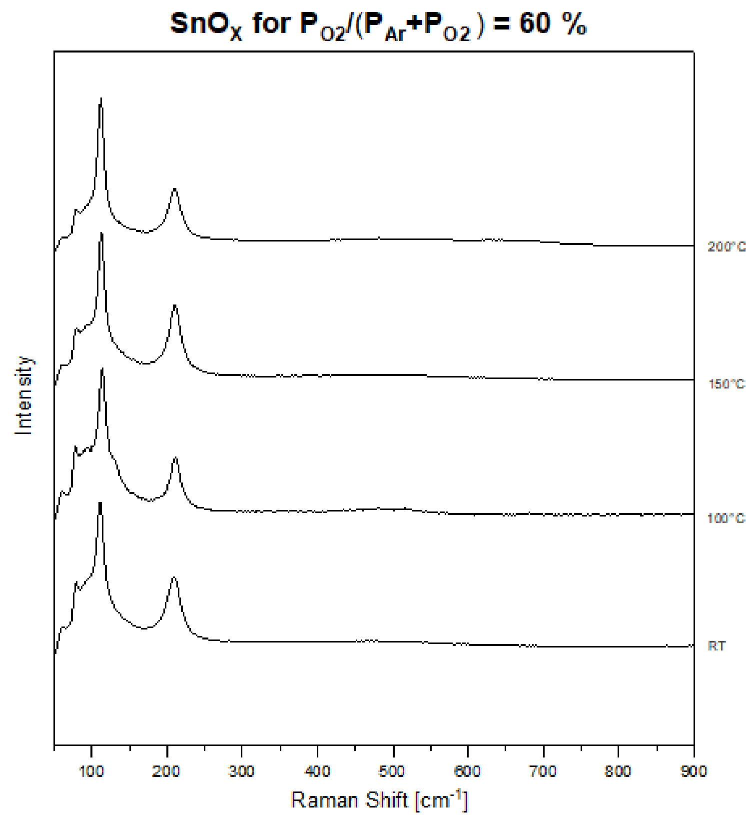

Figure 4.8: Raman spectra of the sputter deposited SnO_x films grown with $p_{O2}/(p_{O2}+p_{Ar})$ = 60 % films at different temperatures on Si substrates.

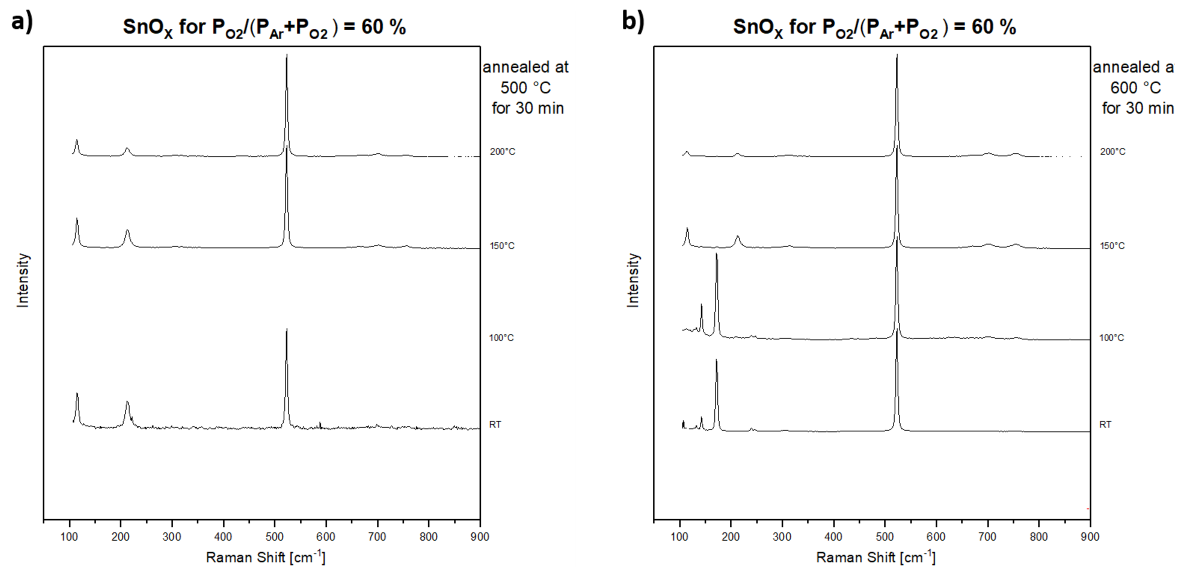

Figure 4.9: Raman spectra of the sputter deposited SnO_X films grown with $p_{O2}/(p_{O2}+p_{Ar})$ = 60 % films at different temperatures on Si substrates in the as deposited condition (RT) and after annealing at **a)** 500 °C and **b)** 600 °C for 30 min.

The Raman spectra for annealed SnO_X films are depicted in **Fig. 4.9**. The measurements worked out for all films except the one deposited at 100 °C and annealed at 500 °C, which did not lead to a conclusive result. All spectra show a very striking peak at a Raman shift at 520.2 ± 0.05 cm^{-1}, which is correlated to the silicon substrate [55]. The peaks corresponding to the SnO phase at 110 cm^{-1} and 210 cm^{-1} are present in most of the spectra. Films annealed at 600 °C after deposition at room temperature and 100 °C (**Fig. 4.9 b)**) show peaks at 140, 170 and 240 cm^{-1} in the Raman spectra, indicating the existence of the Sn_3O_4 phase [53]. The origins of the small recognizable peaks at~700 and 750 cm^{-1} are according to *Guillèn et* al. – see their Raman spectra reported for SnO_X films grow by DC reactive sputter deposition in Fig. 4.10 – the A1g and B2g fundamental vibration modes together with the bands S1-S3 that are activated by disorder in the tin dioxide [53].

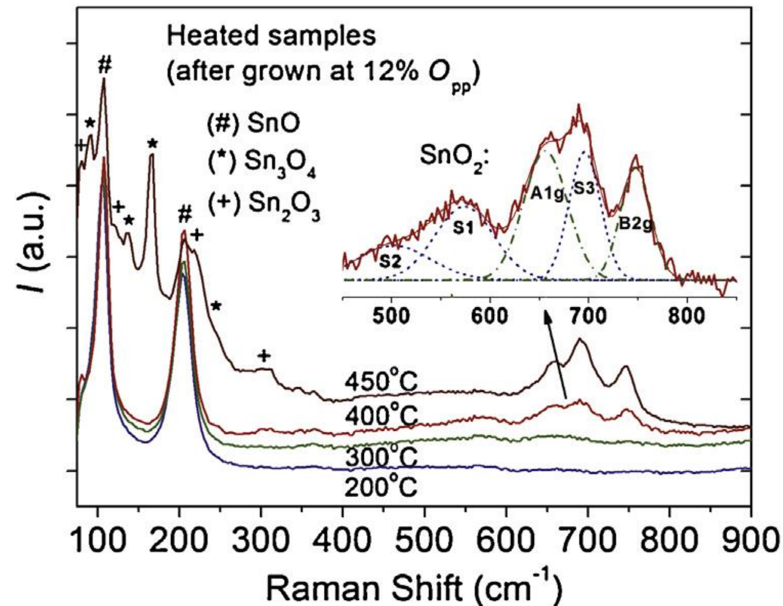

Figure 4.10: Raman spectra for tin oxide layers grown by DC reactive sputter deposition at an oxygen partial pressure of 12 % and annealed in air at different temperatures for 30 min [53].

The comparison of the observed Raman spectra and the X-ray diffractograms enable to draw some conclusions about the phase composition of the films. Due to the overlapping of some peaks corresponding to more than one phases, the XRD patterns gave just hints about the phases present in the SnO_X films. The Raman spectra enable to attribute the observed peaks to SnO, SnO_2 und Sn_3O_4. At this point it is necessary to mention that Raman spectroscopy provides the advantage to investigate amorphous structures, whereas XRD does not[42]. The films grown at oxygen partial pressures above 60 % did not show conclusive Raman spectra.

The impact of annealing the samples is well recognizable for all the films. For the films annealed at 600 °C, an influence of the deposition temperature is noticeable. As mentioned in section **2.1.3**, SnO tends to be oxidized to SnO_2 when heated above a certain temperature by either the formation of the intermediates Sn_2O_3 and Sn_3O_4 or directly (**Fig. 2.1**) [7, 8]. The Raman spectra of the films deposited at 150 °C and 200 °C and annealed at 600 °C show evidence of the existence of SnO_2. This results probably from a direct transformation of SnO into SnO_2, whereas in those films deposited at RT and 100 °C and annealed at 600 °C on the other hand the formation of the intermediates takes place. Another consequence of the heat treatment is the appearance of signals of the silicon substrates in the Raman spectra. The films are becoming more transparent in the range of the wavelength of the used laser.

Comparing now the results of Raman spectroscopy and XRD measurements including the information obtained by ERDA and bringing them together, one has to conclude that in as

deposited tin oxide films with a $p_{O2}/(p_{O2}+p_{Ar})$ of 60 % mainly the SnO phase can be found. Pure tin and tin dioxide are either present in low concentrations, or do not even exist. For receiving SnO_2, a heat treatment of the as deposited films is necessary.

To summarize, tin oxide films were successfully deposited on Si substrates. ERDA measurements reveal that films without any serious contaminations and a largely homogeneous depth profile have been deposited. Combining the results of ERDA and XRD, it can be assumed that for a $p_{O2}/(p_{O2}+p_{Ar})$ ratio below 70 % the as deposited films consist mostly of tin monoxide with some traces of pure tin and provide a crystalline structure for elevated deposition temperatures. For a $p_{O2}/(p_{O2}+p_{Ar})$ ratio above 85 %, the main fraction of the films is assumed to be tin dioxide and the films are characterized by an amorphous structure. Heat treatment in air results in transformation of the amorphous into a crystalline structure,. XRD investigations not exactly reveal which phases are dominant in the annealed films, but based on results obtained by Raman spectroscopy it is assumed that after annealing SnO_2 is the prevalent phase. SnO seems to transform into SnO_2 in an oxidizing atmosphere at 500 °C and above.

4.4 Electrical Resistance

The measurement of the electrical resistance of the tin oxide films was done by a four-point measurement system. For films deposited with $p_{O2}/(p_{O2}+p_{Ar})$ above 60 %, the electrical resistance was not measurable with the used method and system, respectively, indicating an insulating nature of the films. A similar behavior was obtained for the annealed samples, except for the $p_{O2}/(p_{O2}+p_{Ar})$ = 60 % film deposited at 100 °C and annealed at 600 °C. The results of the resistance measurement for all other films are depicted in **Fig. 4.11**. The electrical resistance of films deposited with $p_{O2}/(p_{O2}+p_{Ar})$ = 25 % was taken from former investigations on reactive sputtered tin oxide films using the same deposition system and parameters [56].

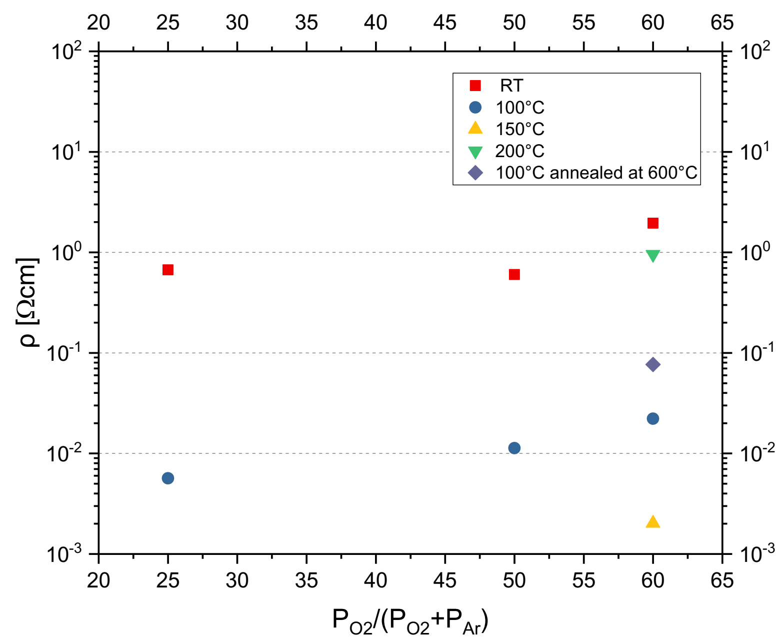

Figure 4.11: Specific electrical resistance of the tin oxide films sputter deposited on Si substrates at different $p_{O2}/(p_{O2}+p_{Ar})$ relations and deposition temperatures.

Regarding the evolution of the specific electrical resistance of the films deposited at room temperature, there is no clear tendency notable how the resistance changes by varying the oxygen partial pressure. The films deposited at 100 °C show an increase of the resistance with increasing oxygen partial pressure. Also, an influence of different deposition temperatures is only notable for the films deposited with $p_{O2}/(p_{O2}+p_{Ar})$ = 25 % and 50 %, where the values of the films deposited at room temperature is higher than for the films deposited at 100 °C. For the films deposited with $p_{O2}/(p_{O2}+p_{Ar})$ = 60 %, no trend is distinguishable about how the deposition temperature influences the electrical resistance of the films. The values for specific electrical resistance vary over several orders of magnitude and correlate partially with values found in literature for SnO_x films, which reach from 0.59 Ωcm (prepared by chemical vapor deposition) to 1.25 Ωcm (prepared reactive DC magnetron sputtering, pure Sn target) and 11.11 Ωcm (prepared by reactive RF magnetron sputtering, SnO/Sn target) [53, 57, 58].

4.5 Gas Sensitivity Measurements

Three films with a $p_{O2}/(p_{O2}+p_{Ar})$ of 60, 70 and 80 % were deposited at chips provided by the MCL. The chips are first covered with a negative resist layer (nLOF) and afterwards via photo lithography the area for the sensing film is opened. In a second step, sputter deposition of the SnO_X films takes place. The final step is the lift off of the resist layer covered with the SnO_X film on it. Thus, a gas sensing film remains at the desired position at the chip. **Figure 4.12** shows the chips with the gas sensing film before (bottom row) and after the lift off (upper row) with a detail view on the gas sensing area deposited on four electrodes.

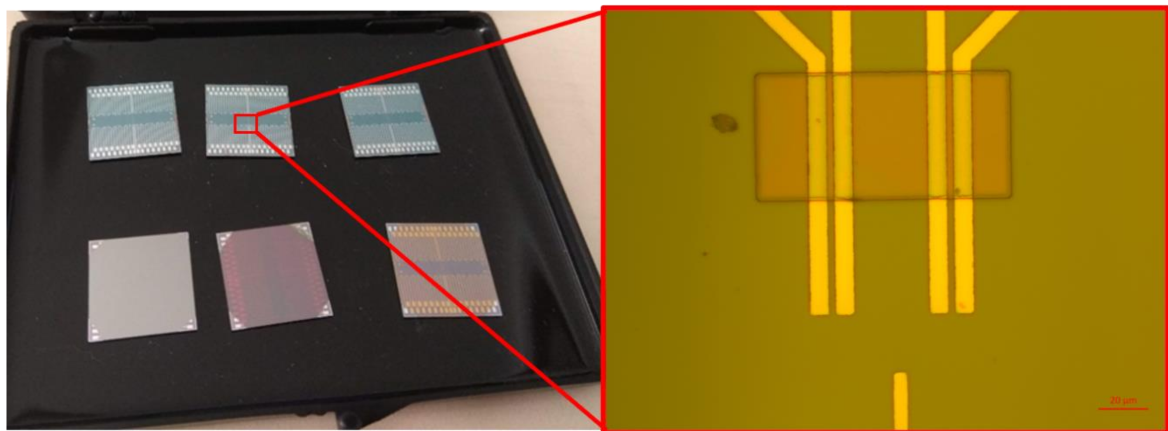

Figure 4.12: The chips for the gas sensing measurement of the SnO_X films before (bottom row) and after the lift off (upper row) and a detailed view of the constellation of the electrodes covered with the remaining gas sensing film.

One chip contains 16 sensors. The principle of the measurement is the same as in the four-point resistivity measurement described in section **3.2.6**. In presence of gas molecules which the gas sensing film is sensitive to, the measured resistance of the gas sensing film changes and the information is transformed into an electrical signal. The gas measurements were performed at 400 °C. After annealing in air at 400 °C for 60 min, a 5 min pulse of CO (50 ppm diluted in nitrogen) was applied to the sensors followed by 15 min of recovery. For the second pulse of 5 min, a hydrocarbon gas mixture (HCMix, with 50 ppm of hydrocarbons diluted in nitrogen) consisting of ethane, ethene, ethyne and propane was used. The whole process was carried at a relative humidity of 50 %. The results of the gas sensitivity measurements are shown in **Fig. 4.13**.

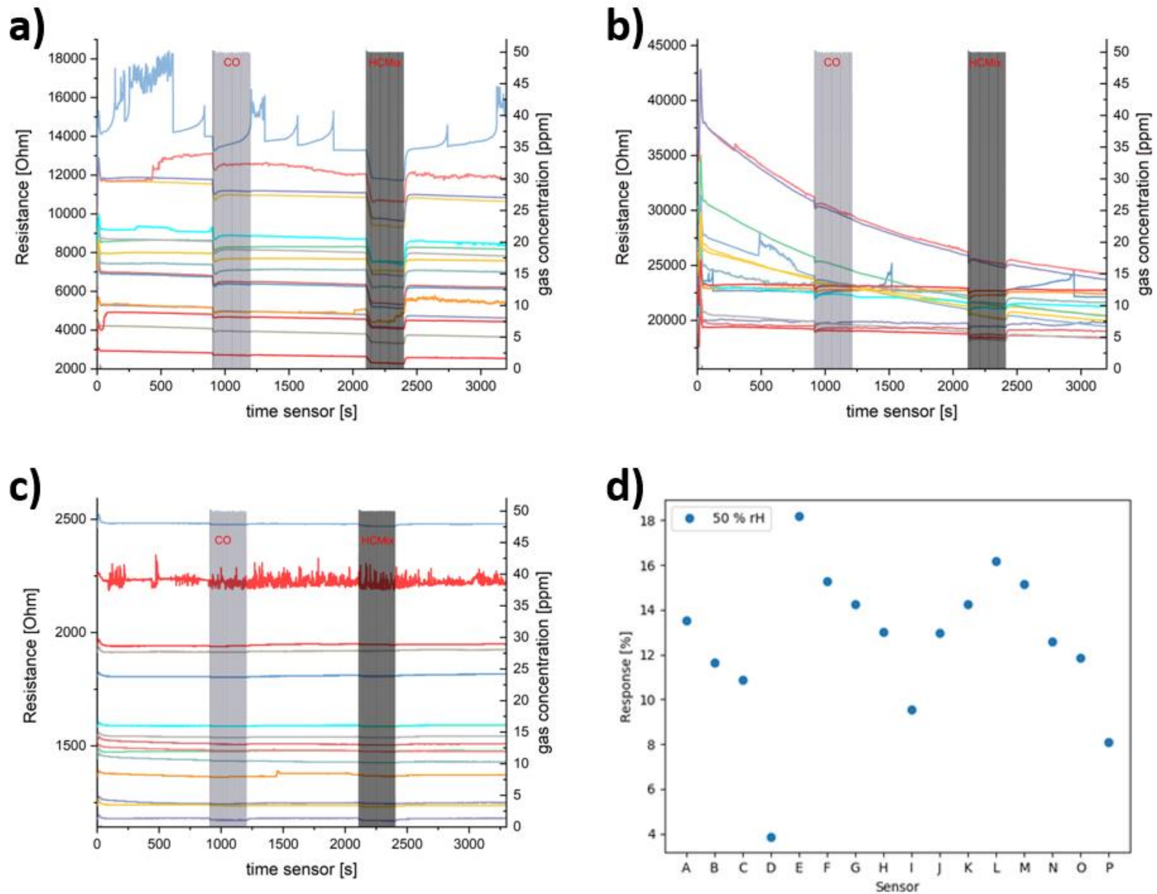

Figure 4.13: Change of the electrical resistance of the gas sensors over the time. **a)** SnO_X with $p_{O2}/(p_{O2}+p_{Ar})$ = 60 %. **b)** SnO_X with $p_{O2}/(p_{O2}+p_{Ar})$ = 70 %. **c)** SnO_X with $p_{O2}/(p_{O2}+p_{Ar})$ = 80 %. The different colored lines indicate the different sensors on the chip. The light grey bar indicates the CO pulse and the dark grey bar indicates the HCMix pulse. **d)** The response of the individual sensors A – P to the HCmix of the 60 % film.

Comparing the changes in resistance of the individual films it is clearly visible, that the films are more sensitive to HCMix than to CO. The sensitivity of the films decreases with increasing oxygen content in the films. In **Fig. 4.13 d)** the relative response S_p of the film deposited with $p_{O2}/(p_{O2}+p_{Ar})$ = 60 % is depicted. The response is calculated as follows:

$$S_p[\%] = \frac{|R_{air}+R_{gas}|}{R_{gas}}, \qquad (8)$$

where R_{air} is the resistance of the film in air and R_{gas} is the resistance of the film in air including the target gas. The mean response $\overline{S}_P$ of the individual films is listed in **Tab 4.3**. Whereas the film with a $p_{O2}/(p_{O2}+p_{Ar})$ = 60 % shows a good response - especially to the HCMix - the response of the film $p_{O2}/(p_{O2}+p_{Ar})$ = 80 % is barely notable.

Table 4.3: Mean response of the SnO_x films grown at different oxygen partial pressure ratios to the target gases CO and HCMix.

	$p_{O2}/(p_{O2}+p_{Ar})$ = 60 %	$p_{O2}/(p_{O2}+p_{Ar})$ = 70 %	$p_{O2}/(p_{O2}+p_{Ar})$ = 80 %
$\bar{S}_P$ to CO [%]	4.06	2.15	0.21
$\bar{S}_P$ to HCMix [%]	12.58	3.31	0.41

4.6 Deposition of Au clusters

Within a first experimental approach done within this thesis, deposition of Au nano clusters via gas phase synthesis was simulated by depositing the clusters in the magnetron sputter system "Josefine II", also used for the deposition of the tin oxide films. The depositions parameters were adjusted in a way that not a continuous Au film would be deposited, but Au clusters on the surface of SnO_X films grown on Si substrates. Albeit in this case it is unknown whether the clusters form in the gas phase or at the substrates´ surface, it was possible to deposit Au clusters. Assuming island growth (see section **2.2**) of Au on tin oxide, the experimental approach was based on using low magnetron currents and very short deposition times to prevent formation of a continuous Au film. The choice of the parameters was based on former studies at the Chair of Functional Materials and Materials Systems. **Tab 4.4** provides an overview on the set values for Ar gas flow, current and deposition time of the individual samples of Au clusters. Before deposition, the chamber was evacuated to a pressure of ~ 10^{-3} Pa. The pressure during deposition was impossible to note, because of the short deposition time. The deposition time was steered manually by opening and closing the shutter.

Table 4.4 Overview on the used parameters to deposit Au clusters.

Sample	Ar Flow [sccm]	Deposition Time [s]	Current [A]
Au1	200	10	0.05
Au2	30	4	0.05
Au3	90	4	0.05

After a first look at the samples using an optical microscope, a continuous film was observed to be formed for sample Au1. On the samples Au2 and Au3, no evidence of Au clusters or film formation was noticeable using the optical microscope. Further, the samples were investigated by AFM, where topography and phase contrast images were taken (**Fig. 4.14**).

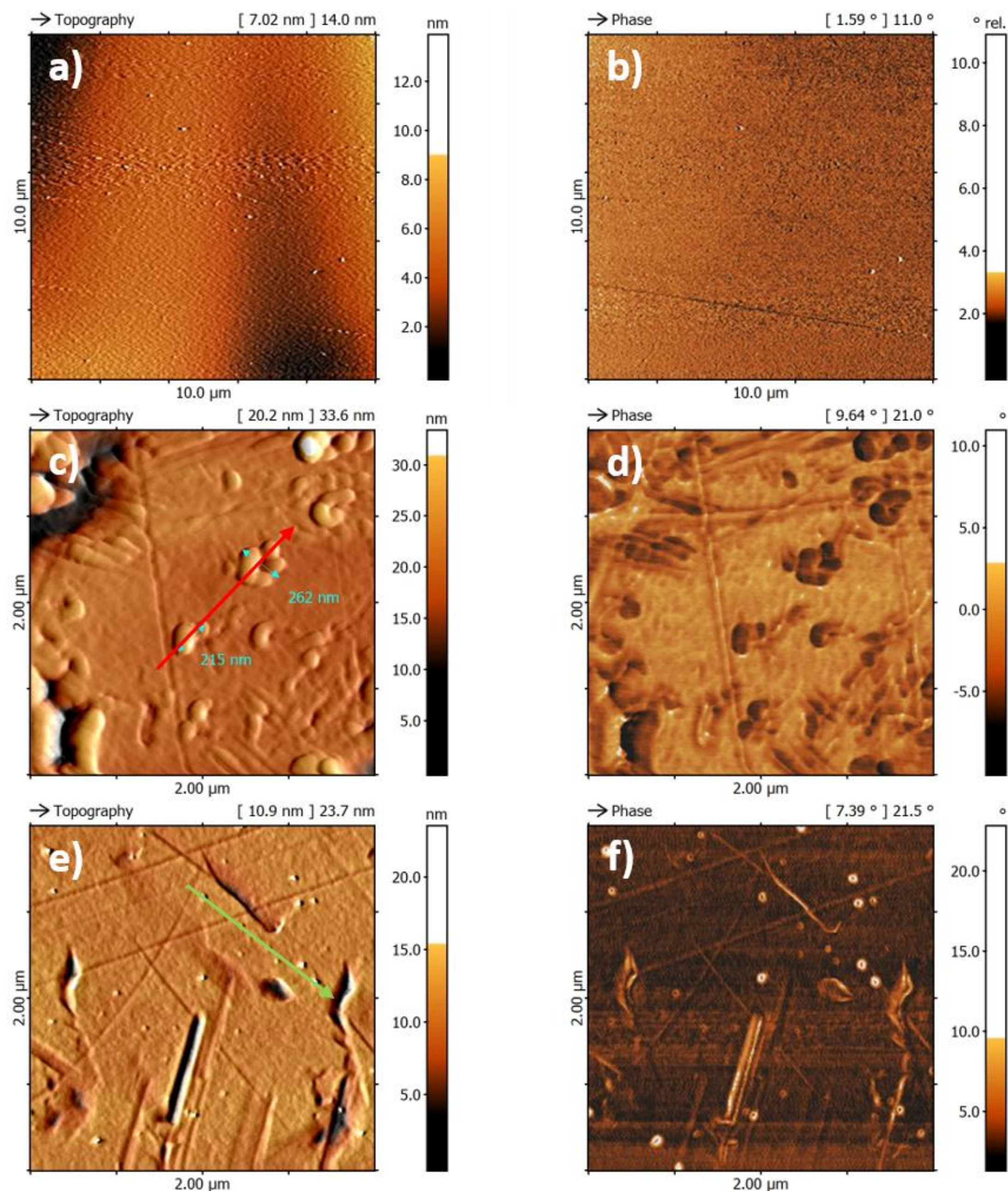

Figure 4.14: AFM images of the Au cluster deposition on SnO_X films on Si substrates ($p_{O2}/(p_{O2}+p_{Ar})$ = 80 %). **a)** Topography and **b)** Phase contrast image of Au1. **c)** Topography and **d)** Phase contrast image of Au2. **e)** Topography and **f)** Phase contrast image of Au3. Along the arrows a height profile was recorded. The lines on the images stem from scratches on the substrate surface.

For sample Au1, the AFM topography (**Fig. 4.14 a)**) and phase contrast images (**Fig. 4.14 b)**) unambiguously reveal that a continuous homogeneous Au film was deposited. This indicates that the chosen parameters do not allow to deposit Au clusters. On the samples Au2 (**Fig. 4.14 c)**) and Au3 (**Fig. 4.14 e)**), discontinuities in form of droplet-like clusters were observed by AFM. Phase contrast images of these two samples (**Fig. 4.14 d)** and **Fig. 4.14 f)**) provide evidence, that the material of the clusters is not the same as the substrate. Thus, it can be

assumed that Au clusters have been formed. As the aim of the experiment was to simulate the deposition of Au clusters in the range of a few nanometers via gas phase synthesis, the size of the clusters has been characterized by taking line profiles along the red arrow visible for Au2 in **Fig. 4.14 c)** and the green arrow in **Fig. 4.14 e)**. **Fig. 4.15** indicates that the height of the clusters does not differ significantly, whereas their diameter shows some significant differences. The Au2 clusters are splotch-like with diameters of over 200 nm (consider the different length scale in **Fig. 4.15** for vertical and horizontal axis). Thus, the formed clusters can not be considered as nano-sized. Nevertheless, with diameters between 20 and 100 nm, the Au3 clusters are smaller than those of the Au2. The reason therefore could be that increasing pressure leads enhanced scattering of sputtered Au atoms in the gas phase and consequently to a higher number of newly formed clusters on the substrate surface.

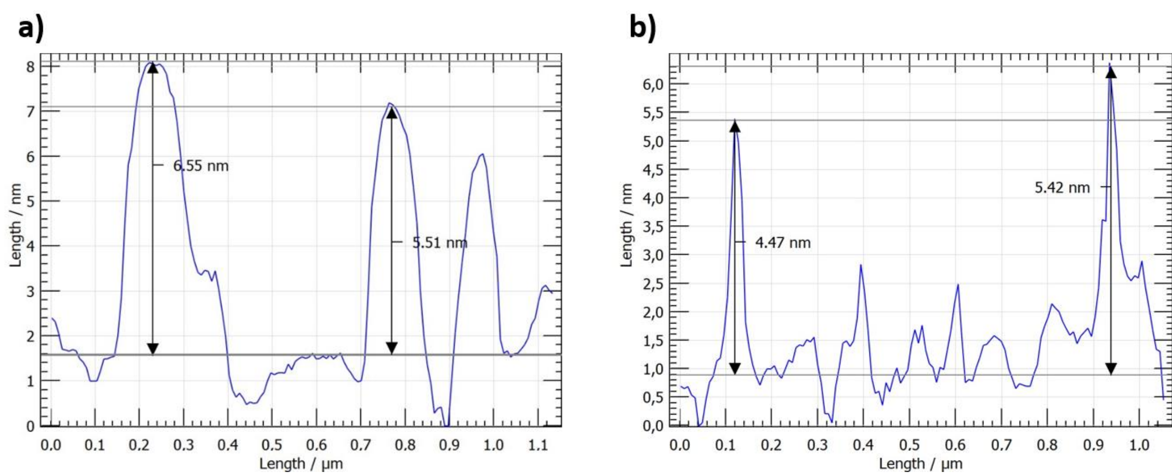

Figure 4.15: The corresponding height profiles of the samples **a)** Au2 and **b)** Au3 along the red respectively green arrow in the topography images in **Fig. 4.14**.

According to the definition of nano structured materials (sizes < 100 nm) [59], the deposited Au3 clusters are considered to be nano clusters. Whether the formation takes place in the gas phase or on substrate surface cannot be determined. It is more likely, that the clusters nucleated at the surface and further growth took place, since the Au1 sample provided a continuous and homogeneous surface nearly without any roughness. The intention of the approach done within this thesis was to fabricate Au nano clusters by DC magnetron sputtering, which seems to be possible by choosing the right parameters. However, the reproducibility for this process has not been evaluated within this thesis and has to be assumed to be questionable. The deposition time was steered manually by opening and closing the shutter in front of the magnetron, which adds – taking into account the short deposition time of 10 s – some uncertainty to the process. Further, the size distribution as well

as the particle number per area are assumed to not be uniform. For the reproducible deposition of nano clusters, a more sophisticated method like gas phase synthesis equipped with mass filters for uniform size distribution are indispensable.

5 Conclusions and Outlook

5.1 Conclusions

Within this work, tin oxide thin films for the application in gas sensing devices were synthesized via reactive DC magnetron sputtering with varying the composition of the argon/oxygen (Ar/O_2) atmosphere in the vacuum chamber during the deposition process. The aim was to design a process allowing a deposition of SnO_X films without organic contaminations stemming e.g. from spray pyrolysis, which is suitable for the state-of-the-art process chain in sensor fabrication.

The coatings were studied concerning their dependency of structure, elemental and phase composition on the oxygen partial pressure $p_{O2}/(p_{O2}+p_{Ar})$ and different deposition temperatures. The set oxygen partial pressure was in the range of 50 to 90 %. Further, the change of phase composition during an annealing process was evaluated. Elastic recoil detection analysis measurements yielded O/Sn atomic ratios ranging from 0.87 for $p_{O2}/(p_{O2}+p_{Ar})$ = 60 % to 2.18 for $p_{O2}/(p_{O2}+p_{Ar})$ = 90 %, indicating a shift from nearly stoichiometric SnO films to nearly stoichiometric SnO_2 films in the range of the set oxygen partial pressure. The O/Sn ratio of the 90 % film was nearly exact the same as that for a film deposited via spray pyrolysis, which was in previous studies at the Materials Center Leoben successfully tested as a gas sensing material. X-ray diffraction gave conclusions about the film structure, which is amorphous for deposition at room temperature. For elevated deposition temperatures, films with an oxygen partial pressure < 70 % provide a crystalline structure – most probably SnO with small fractions of SnO_2 and pure tin. By annealing the films in an oxidizing atmosphere, a transformation from amorphous to crystalline structure takes place. Raman spectroscopy reveals that SnO is oxidized to SnO_2 during the annealing process. First gas sensitivity measurements show that the sensitivity to the used target gases decreases with increasing oxygen partial pressure during film deposition.

5.2 Outlook

The studies on reactively sputtered SnO_X films within this work can contribute to implement the sputtering process into the gas sensor fabrication chain. At high $p_{O2}/(p_{O2}+p_{Ar})$ ratios, SnO_2 films, which are widely investigated as a gas sensing material, of a very high cleanliness can be synthesized. To complete structural investigations, transmission electron microscopy or X-ray photoelectron spectroscopy would be necessary to get more conclusive information about

the Sn-O bonding and to distinguish between SnO and SnO_2. Next step would be to do intensive studies on the gas sensing behaviour of the reactively sputter deposited SnO_X films and to optimize the $p_{O2}/(p_{O2}+p_{Ar})$ ratio during deposition to improve their functionality as a gas sensing material.

Forward-looking, gas phase synthesis provides a very promising method to produce nano clusters of a discrete size and particle per area density. This should make possible to tailor the gas sensing behaviour of solid-state gas sensors by successively improving the deposition parameters. Once the process is well understood and controllable, nano cluster functionalized solid-state gas sensors could be state of the art and found in everyday life devices.

References

[1] Franke, M. E. ; Koplin, T. J. ; Simon, U.: *Metal and Metal Oxide Nanoparticles in Chemiresistors: Does the Nanoscale Matter?* In: *Small* 2 (2006), pp. 36–50

[2] Mattox, D. M.: *Handbook of physical vapor deposition (PVD) processing*. 2nd ed. Oxford, UK : William Andrew, 2010 pp. 237-357

[3] Grammatikopoulos, Panagiotis ; Steinhauer, Stephan ; Vernieres, Jerome ; Singh, Vidyadhar ; Sowwan, Mukhles: *Nanoparticle design by gas-phase synthesis*. In: *Advances in Physics: X* 1 (2016), Nr. 1, pp. 81–100

[4] *Technical data for the element Tin in the Periodic Table*. URL https://periodictable.com/Elements/050/data.html. – Date of actualization: 2017-11-10. 000Z – Retrieved on 2020-07-05

[5] Sawyer, Donald T.: *Oxygen Chemistry* : Oxford University Press, 1991, pp. 3-17

[6] Batzill, Matthias ; Diebold, Ulrike: *The surface and materials science of tin oxide*. In: *Progress in Surface Science* 79 (2005), 2-4, pp. 47–154

[7] Lawson, F.: *Tin Oxide—Sn_3O_4*. In: *Nature* 215 (1967), Nr. 5104, pp. 955–956

[8] Murken, G. ; Tromel, M.: *Ueber das bei der Disproportionierungvon SnO entstehende Zinnoxid, Sn_2O_3*. In: *Z. Anorg. Allg. Chem.* 897 (1973), Nr. 117

[9] Hasselbach, K. ; Murken, G. ; Tromel, M.: *Mössbauer-Messungen an Sn_2O_3*. In: *Z. Anorg. Allg. Chem.* 897 (1973), Nr. 127

[10] Cahen, S. ; David, N. ; Fiorani, J. M. ; Maître, A. ; Vilasi, M.: *Thermodynamic modelling of the O–Sn system*. In: *Thermochimica Acta* 403 (2003), Nr. 2, pp. 275–285

[11] Pannetier, J. ; Denes, G.: *Tin(II)oxide: structure refinement and thermal expansion*. In: *Acta Crystallogr.* 36 (1980), Nr. 2763

[12] Ogo, Yoichi ; Hiramatsu, Hidenori ; Nomura, Kenji ; Yanagi, Hiroshi ; Kamiya, Toshio ; Hirano, Masahiro ; Hosono, Hideo: *p-channel thin-film transistor using p-type oxide semiconductor, SnO*. In: *Applied Physics Letters* 93 (2008), Nr. 3, p. 32113

[13] Togo, A. ; Oba, F. ; Tanaka, I. ; Tatsumi, K.: *First-principles calculations of native defects in tin monoxide*. In: *Physical Review B* 74 (2006), Nr. 19, p. 195128.

[14] Saji, K. J. ; Venkata Subbaiah, Y. P. ; Tian, K. ; Tiwari, A.: *P-type SnO thin films and SnO/ZnO heterostructures for all-oxide electronic and optoelectronic device applications*. In: *Thin Solid Films* (2016), Nr. 605, pp. 193–201

[15] LUO, H. ; LIANG, L. Y. ; LIU, Q. ; CAO, H. T.: *Magnetron-Sputtered SnO Thin Films for p-Type and Ambipolar TFT Applications*. In: *ECS Journal of Solid State Science and Technology* 3 (2014), Nr. 9, Q3091-Q3094.

[16] HWANG, S. ; KIM, Y. Y. ; LEE, J. H. ; SEO, D. K. ; CHO, H. K.: *Irregular electrical conduction types in tin oxide thin films induced by nanoscale phase separation*. In: *American Ceramic Society* (2012), Nr. 95, pp. 324–327

[17] BOLZAN, A. A. ; FONG, C. ; KENNEDY, B. J. ; HOWARD, C. J.: *Structural studies of rutile-type metal dioxides*. In: *Acta Crystallographica Section B: Structural Science* 53 (1997), Nr. 3, pp. 373–380.

[18] VELMATHI, G. ; MOHAN, S. ; HENRY, Rabinder: *Analysis and Review of Tin Oxide-Based Chemoresistive Gas Sensor*. In: *IETE Technical Review* 33 (2016), Nr. 3, pp. 323–331

[19] STEINHAUER, Stephan: *Gas Sensing Properties of Metal Oxide Nanowires and their CMOS Integration*. PhD Thesis

[20] CHANG, S.-C.: *Oxygen chemisorption on tin oxide: Correlation between electrical conductivity and EPR measurements*. In: *Journal of Vacuum Science and Technology* 17 (1980), Nr. 366

[21] KOROTCENKOV, G. ; CHO, B. K. ; GULINA, L. B. ; TOLSTOY, V. P.: *Gas sensor application of Ag nanoclusters synthesized by SILD method*. In: *Sensors and Actuators B: Chemical* 166-167 (2012), pp. 402–410

[22] WÖLLENSTEIN, J. ; BÖTTNER, H. ; JAEGELE, M. ; BECKER, W. J. ; WAGNER, E.: *Material properties and the influence of metallic catalysts at the surface of highly dense SnO_2 films*. In: *Sensors and Actuators B* (2000), Nr. 70, pp. 196–202

[23] OHRING, Milton: *Materials science of thin films* : *Deposition and structure*. 2nd ed. San Diego CA : Academic Press, 2002, pp. 357-504

[24] SREE HARSHA, K. S.: *Principles of Physical Vapor Deposition of Thin Films* : Elsevier, 2005, pp. 552-804

[25] WASA, Kiyotaka ; KANNO, Isaku ; KOTERA, Hidetoshi: *Handbook of sputter deposition technology* : *Fundamentals and applications for functional thin films, nanomaterials and MEMS*. 2nd ed. Waltham MA : William Andrew, 2012, pp. 4-302

[26] BUNSHAH, Rointan F.: *Handbok of Hard Coatings* : Noyes, New Jersey, 2001, pp. 4-7

[27] ROSSNAGEL, Stephen M. ; CUOMO, Jerome J. ; WESTWOOD, William D.: *Handbook of Plasma Processing Technology* : *Fundamentals, Etching, Deposition and Surface Interactions* : Noyes Publications, 1990, pp. 233-240

[28] VOSSEN, John L. ; KERN, Werner: *Thin Film Processes II* 1991, pp. 88-183

[29] VENABLES, John A.: *Introduction to Surface and Thin Film Processes* : Cambridge University Press, 2003, pp. 144-147

[30] WASA, Kiyotaka ; KITABATAKE, Makoto ; ADACHI, Hideaki: *Thin film materials technology* : *Sputtering of compound materials*. Norwich NY, Heidelberg : William Andrew Pub.; Springer, 2004, pp. 17-23

[31] MOVCHAN, B. A.: *Study of the structure and properties of thick vacuum condensates of nickel, Titanium, Tungsten, Aluminium Oxide and Zirconium Dioxide*. In: *Phys. Met. Metallogr.* 28 (1969), Nr. 4, pp. 83–90.

[32] THORNTON, John A.: *High Rate Thick Film Growth* (1977), pp. 239-260

[33] AUCIELLO, O.: *Multicomponent and multilayered thin films for advanced microtechnologies: Techniques, fundamentals, and devices*. Springer Science+Business Media Dordrecht (1993)

[34] ADAMIK, M. ; BARNA, P.B.: Formation and characterization of the structure of surface coatings. In: *Pauleau Y.; Barna P.B.; Protective Coatings and Thin Films. p. 279-297. Kluwer Acedemic Publishers. 1997*.

[35] BISWAS, A. ; BAYER, I. S. ; BIRIS, A. S. ; WANG, T. ; DERVISHI, E. ; FAUPEL, F.: *Advances in top-down and bottom-up surface nanofabrication: techniques, applications and future prospects*. In: *Adv. Colloid Interface Sci.* (2012), Nr. 170, pp. 2–27

[36] WEGNER, K. ; PISERI, P. ; TAFRESHI, H. Vahedi ; MILANI, P.: *Cluster beam deposition: a tool for nanoscale science and technology*. In: *Journal of Physics D: Applied Physics* 39 (2006), Nr. 22, R439-R459

[37] KYLIÁN, Ondřej ; PROKEŠ, Jan ; POLONSKYI, Oleksandr ; ČECHVALA, Juraj ; KOUSAL, Jaroslav ; PEŠIČKA, Josef ; HANUŠ, Jan ; BIEDERMAN, Hynek: *Deposition and characterization of Pt nanocluster films by means of gas aggregation cluster source*. In: *Thin Solid Films* 571 (2014), pp. 13–17

[38] XIROUCHAKI, C. ; PALMER, R. E.: *Deposition of size-selected metal clusters generated by magnetron sputtering and gas condensation: a progress review*. In: *Philosophical transactions. Series A, Mathematical, physical, and engineering sciences* 362 (2004), Nr. 1814, pp. 117–124

[39] GRANQVIST, C. G. ; BUHRMANN, R. A.: *Ultrafine metal particles*. In: *Journal of Physics* (1976), Nr. 5, pp. 2200-2219

[40] FLAGAN, R. C. ; LUNDEN, M. M.: *Particle structure control in nanoparticle synthesis from the vapor phase*. In: *Materials Science and Engineering A* (1995), Nr. 204, pp. 113–124

[41] BRANDON, D. ; KAPLAN, Wayne D.: *Microstructural Characterization of Materials* : *2nd Edition* : John Wiley & Sons, Ltd, 2008, pp. 55-90

[42] LARKIN, Peter: *Infrared and Raman Spectroscopy* : *Principles and Spectral Interpretation*. 1st : Elsevier, 2011, pp. 1-17

[43] LONG, D. A.: *Raman Spectroscopy*. New York : McGraw-Hill, 1977

[44] TIRIRA, J. ; SERRUYS, Y. ; TROCELLIER, P.: *Forward Recoil Spectrometry* : *Applications to Hydrogen Determination in Solids* : Plenum Press, 1996, pp. 1-40

[45] ASSMANN, W. ; HUBER, H. ; STEINHAUSEN, Ch. ; DOBLER, M. ; GLÜCKLER, H. ; WEIDINGER, A.: *Elastic recoil detection analysis with heavy ions*. In: *Nuclear Instruments and Methods in Physics Research Section B: Beam Interactions with Materials and Atoms* (1994)

[46] THOMPSON, Richard L.: *Surface and Interfacial Characterization* : *Ion Beam Analysis*. URL https://www.researchgate.net/publication/235684707 (September 2020)

[47] STRUB, Erik: *Materials analysis with heavy ions*, 2005. URL https://www.researchgate.net/publication/277987991 (September 2020)

[48] KRUSE, O. ; CARSTAJEN, H. D.: *High-depth resolution ERDA of H and D by means of an electrostatic spectrometer*. In: *Nuclear Instruments and Methods in Physics Research Section B* (1994), Nr. 89, pp. 191–199

[49] BARRADAS, N.P. ; JEYNES, C. ; WEBB, R.P. In: *Applied Physics Letters* 71 (1997), Nr. 291

[50] GIANNUZZI, Lucille A. ; PRENITZER, Brenda I. ; KEMPSHALL, Brian W.: Ion-Solid Interactions. In: GIANNUZZI, Lucille A.; STEVIE, Fred A. (Hrsg.): *Introduction to Focused Ion Beams* : *Instrumentation, Theory, Techniques and Practice*. Springer Science+Business (2005) pp. 13-53

[51] GUZMÁN-CABALLERO, D. E. ; QUEVEDO-LÓPEZ, M. A. ; RAMÍREZ-BON, R.: *Optical properties of p-type SnOx thin films deposited by DC reactive sputtering*. In: *Journal of Materials Science: Materials in Electronics* 30 (2019), Nr. 2, pp. 1366–1373

[52] CHEN, Z. ; XIAO, X. ; SHAO, Y. ; MENG, W. ; ZHANG, S. ; YUE, L ; XIE, L. ; ZHANG, P. ; LU, H.: *Fabrication of p-Type copper oxide thin-film transistors at different oxygen partial pressure*. Piscataway, NJ : IEEE, 2014, pp. 1-3

[53] GUILLÉN, C. ; HERRERO, J.: *P-type SnO thin films prepared by reactive sputtering at high deposition rates*. In: *Journal of Materials Science & Technology* 35 (2019), Nr. 8, S. 1706–1711, pp. 1706-1711

[54] LUO, Hao ; LIANG, Ling Yan ; CAO, Hong Tao ; LIU, Zhi Min ; ZHUGE, Fei: *Structural, Chemical, Optical, and Electrical Evolution of SnOx Films Deposited by Reactive rf Magnetron Sputtering*. In: *ACS Applied Materials & Interfaces* 4 (2012), Nr. 10, pp. 5673–5677

[55] PARKER, J. H. ; FELDMAN, D. W. ; ASHKIN, M.: *Raman Scattering by Silicon and Germanium*. In: *Physical Review* 155 (1967), Nr. 3, pp. 712–714.

[56] TERZIYSKA, V. L. ; MITTERER, C.: *Project Report - Nanosensors* 2019

[57] JIANG, Yinzhu ; SUN, Wenping ; XU, Bin ; YAN, Mi ; BAHLAWANE, Naoufal: *Unusual enhancement in electrical conductivity of tin oxide thin films with zinc doping*. In: *Physical chemistry chemical physics : PCCP* 13 (2011), Nr. 13, pp. 5760–5763

[58] KIM, Cheol ; KIM, Sungdong ; KIM, Sarah Eunkyung: *Transparent SnOx thin films fabricated by radio frequency reactive sputtering with a SnO/Sn composite target*. In: *Thin Solid Films* 634 (2017), pp. 175–180

[59] ISO/TS 80004-1:2015. 2015. *Nanotechnologies -- Vocabulary -- Part 1: Core terms.*